To the Graduate Council:

I am submitting herewith a thesis written by Karla Marie Swift entitled "An Experimental Analysis of The Laminar Separation Bubble At Low Reynolds Numbers." I have examined the final electronic copy of this thesis for form and content and recommend that it be accepted in partial fulfillment of the requirements for the degree of Master of Science with a major in Aerospace Engineering.

Ahmad Vakili, Major Professor

We have read this thesis
and recommend its acceptance:

Basil Antar

U. Peter Solies

Accepted for the Council:

Carolyn R. Hodges
Vice Provost and Dean of the Graduate School

(Original signatures are on file with official student records.)

AN EXPERIMENTAL ANALYSIS OF THE LAMINAR SEPARATION BUBBLE AT LOW REYNOLDS NUMBERS

A THESIS
PRESENTED FOR THE
MASTER OF SCIENCE
DEGREE
THE UNIVERSITY OF TENNESSEE SPACE INSTITUTE

KARLA MARIE SWIFT
DECEMBER 2009

Acknowledgments

The completion of this paper, and thus my master's degree, not only represents a personal academic accomplishment but the steadfast support of many. I cannot express enough gratitude to my advisor, Dr Ahmad Vakili, whose enthusiasm and guidance were the foundation to the success of this project. Throughout the coursework and this project, his genuine concern for students and their quality of education was consistent and much appreciated.

I would like to extend my thanks for the technical support of Jim Goodman and his staff. Specifically Joel Davenport for his help with the calibration and experimental phase and Chris Armstrong for the fabrication of the model and mount. My gratitude for their time, advice and wealth of experience cannot be overstated.

To committee members, Dr Basil Antar and Dr U.Peter Solies, I am very grateful for taking time out of their own busy schedules to provide guidance and advice.

A special thank-you is extended to my parents Greg and Rosemarie for their unwavering support. They had confidence in me even when I did not.

I also need to acknowledge my mother and father in-law, Grant and Maureen for their encouragement. I greatly appreciated the magazine articles, videos and references regarding the subject of unmanned aerial vehicles.

Above all, I am indebted to my best friend and husband David without whose sacrifices, patience and encouragement, I would not be have been able to pursue and succeed in this endeavour.

Abstract

This paper is an investigation into the laminar separation bubble that frequently plagues airborne vehicles operating in the low Reynolds number regime – experimentally found to be typically present in flows with Reynolds numbers below 10^6 (Lissaman 1983). The specific application driving the present investigation is the fixed wing performance of unmanned micro air vehicles (MAVs), defined by their maximum chord length of 6 inches and current cruising speeds of 10-20 meters per second (Mueller 2001). A basic generic model was chosen for this investigation: a circular arc (section of 16 inch diameter PVC pipe) with sharp leading and trailing edges having a chord length of 9.3 inches and height of 1.5 inches. This airfoil model was tested in the UTSI water tunnel at Reynolds numbers of 27,000 and 45,000. The goal of this study was to gain some insight into the boundary layer behaviour through the use of dye injection for flow visualization and hot film anemometry for quantitative velocity measurements. Small diameter cylinders were then statically placed upstream of the model to determine their interaction with the laminar separation bubble and its effects on the boundary layer downstream over the airfoil model. The length and height of the laminar separation bubble was found to be impacted with a small cylindrical wire placed upstream at all Reynolds numbers and angles of attack with the exception of an 18 degree angle of attack at the higher Reynolds number. However, these changes did not result in a substantial or distinguishable improvement in the downstream separation point. The laminar separation bubble was found to be nearly or completely eliminated when a thermocouple wire was placed upstream of the leading edge. Although the elimination of the bubble would result in only a minor decrease in drag and increase in lift, there would be a possible improvement in the stability of the leading edge stall and possible reduction or elimination in the hysteresis associated with stall.

Preface

The purpose of this research is to gain fundamental understanding of laminar bubble behaviour and some insight into their control and its potential impact on the performance of the airfoil. Applications of this study would most likely be in the areas of the flight of Micro Unmanned Aerial Vehicles (MAV) for potential military applications. Without understanding the aerodynamics of the MAV, specifically the low Reynolds number regime, little progress can be made towards reaching the goal of having an air vehicle that can carry enough payload – i.e. avionics, surveillance and communication equipment – for a long enough range to benefit soldiers and/or civilian security forces.

Table of Contents

List of Figures

Nomenclature

b = airfoil span

c_d = coefficient of drag

c_l = coefficient of lift

c_p = coefficient of pressure

H = shape factor

L = length

P = mean pressure in turbulent flow

p = static pressure

$\tilde{p}$ = turbulent flow pressure fluctuation

Re = Reynolds Number

t = time

u = local velocity vector in the x-direction

v = local velocity vector in the y-direction

x = direction parallel to the flow

y = direction perpendicular to the flow

$\tilde{u}$ = turbulent velocity fluctuations

U_t = mean turbulent velocity

U = mean freestream velocity

α = angle of attack

E_{ij} = mean stress tensor

δ = boundary layer thickness

δ* = boundary layer displacement thickness

θ = momentum thickness

ρ = density

μ = viscosity

ν = kinematic viscosity

Chapter 1

INTRODUCTION

Background

Although not a new subject, large scale interest in research into low Reynolds number aerodynamics has began to increase following the evolution of unmanned aircraft systems. The science and technology are continuing to develop rapidly thus allowing the concept of smaller unmanned vehicles to come to fruition. As the size of these flyers, and their associated Reynolds number decreases, engineering challenges of aerodynamics, propulsion, control, avionics, and communication increase (Shyy et al 2008). However, the advantages are numerous thus making the unmanned flyers worthy of the recent myriad of research grants and programs targeted at learning more about this low Reynolds number regime. Continued research and development is thus critical to increase the confidence that the systems can achieve success in their current roles and to expand the scope of their missions for the benefit of security in both military and civilian environments. To overcome the specific aerodynamic challenge, researchers have turned to the "professionals" – birds and insects. This has lead to the emergence of such concepts as flapping wings, hybrid fixed and flapping wings, and rotary wings, in addition to the traditional fixed wing flyer – each concept with it's own design purpose and assets (Shyy et al 2008). The fixed wing micro aerial vehicles (MAVs) are the most efficient and have a better range and endurance than their flapping wing and rotary wing counterparts. Unfortunately, the aerodynamic efficiency of the MAVs is far inferior to the larger, more sophisticated and generally better understood aerodynamics of manned air vehicles.

Low Reynolds Number Aerodynamics

One overwhelming characteristic that has become apparent in the fixed wing type of low Reynolds number flyers is the laminar separation bubble and its effects on aerodynamic performance. Research has shown the presence of short and long bubbles (Tani 1964) to control the aerodynamics characterized by chord Reynolds numbers below 10^5, the precise flight regime in which the MAV finds itself with the 6 inch chord by which it is defined (Mueller 2003). Depending on the length of the separation bubble, drag may be substantially increased and lift decreased because of the altered pressure distribution attributable to the bubble characteristics. In addition, unfavourable abrupt stall and associated hysteresis has also been linked to the laminar separation bubble. The presence and exact behaviour of the bubble is dependant upon airfoil shape, Reynolds number, surface roughness, sound waves and free stream turbulence. A myriad of well-documented experimentation must be carried out and analysed to determine separation bubble behaviour and thus eventually predict and improve the flying qualities of a fixed wing low Reynolds number MAV.

Statement of Objective

The purpose of this research was to analyse the two dimensional fluid flow characterized by the low Reynolds numbers through flow visualization and qualitative velocity measurements in the boundary layer on a generic airfoil model. Specifically, the behaviour of the laminar separation bubble and it's downstream effects were studied with variations in angle of attack, chord Reynolds numbers and with small diameter circular cylinders placed upstream of the leading edge. Chapter 2 explains the theory behind low Reynolds number aerodynamics and analyses the associated governing equations. Chapter 3 describes the experimental approach and set-up while Chapter 4 presents the results and analysis of the water tunnel tests. Finally, Chapter 5 contains conclusions and any recommendations for further research/testing.

Chapter 2

TECHNICAL REVIEW

Theory

The Reynolds Number

Dimensional analysis of the pressure acting on an airfoil shows the Reynolds number appearing as a dominant parameter. Proposed by Osborne Reynolds (1842-1912) in 1883, the Reynolds number has become known to the most important non-dimensional number in fluid dynamics (White 2006). It is a naturally occurring parameter that also appears as a result of non-dimensionalizing the Navier-Stokes equation and has allowed the analysis of dynamically similar flow patterns for objects of similar geometry. The Reynolds number, as calculated below, is a function of fluid density, viscosity, velocity and a reference length and is essentially a ratio of inertial to viscous forces. The lower the Reynolds number, the more influential the viscous forces become.

$$\mathrm{Re} = \frac{UL}{\nu}$$

Figure 1 (Lissaman 1983) shows the range of Reynolds numbers in which general classes of natural and man-made flying objects operate. There are different ranges of Reynolds number for which performance characteristics vary. In aerodynamics, performance quality is typically quantified by the ratio of lift to drag forces, or, in non-dimensional terms (for the sake of generality) the ratio of lift coefficient to drag coefficient. As seen in Figure 2 (Lissaman 1983) a significant change in the lift to drag ratio of typical smooth airfoils occurs at a Reynolds number of approximately 10^5. It is in this transition range that MAVs are operating and researchers/designers must therefore find ways to increase the lift to drag ratio of airfoils to achieve optimal MAV performance. Before that can happen, the fluid mechanics surrounding this low Reynolds number regime must be fully understood.

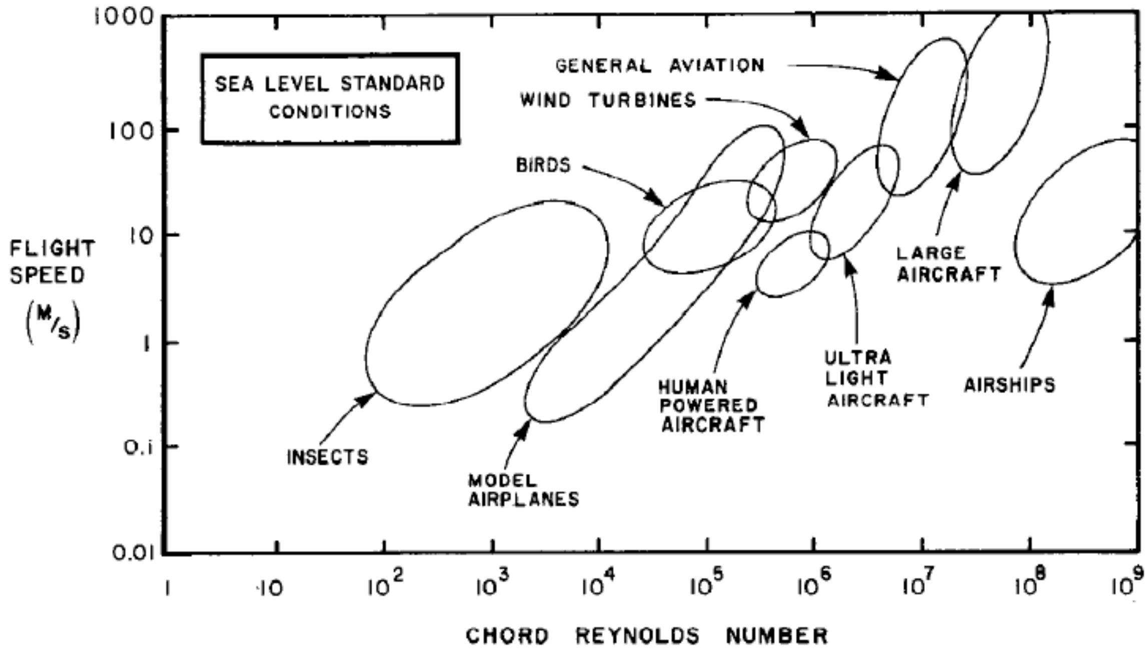

Figure 1. Chord Reynolds Number for Various Classes of Air Vehicles.

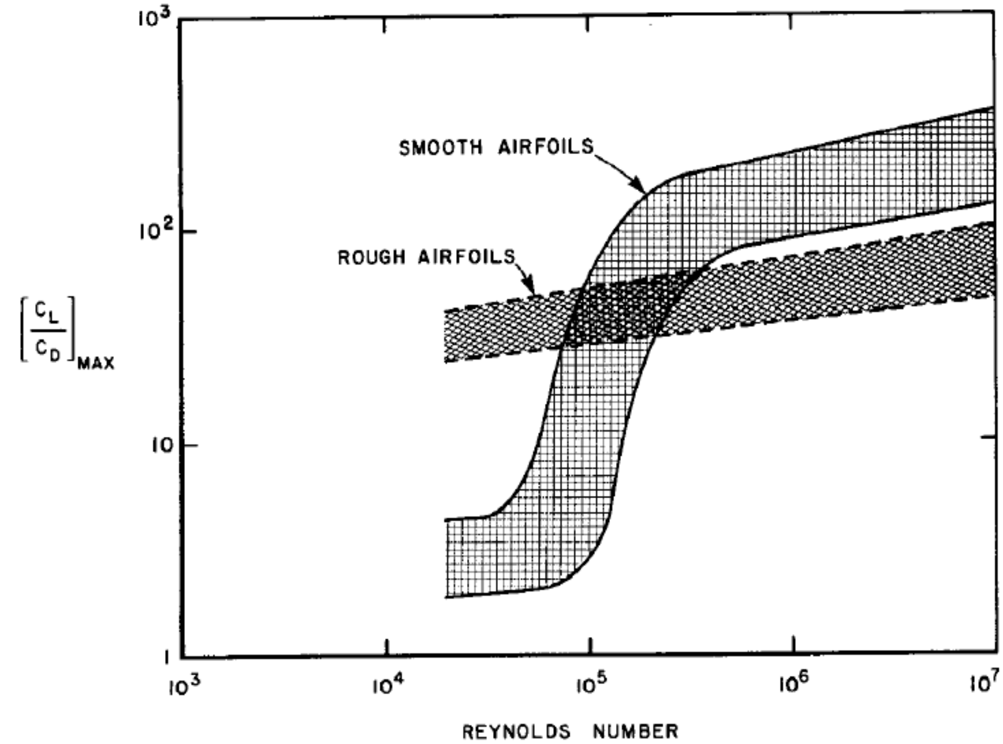

Figure 2. Lift to Drag Ratio as a Function of Reynolds Number.

Boundary Layer Growth

The boundary layer on a surface in a viscous fluid is characterized by a velocity gradient perpendicular to the tangent of the surface. The presence of viscosity dictates a no-slip boundary condition at the surface of the object, meaning the velocity at the surface is zero (White 2006). At some distance away from the surface, the velocity of the flow must match the free stream velocity, thus creating a velocity gradient (shear layer) and defining an approximate boundary layer thickness. Since the transition from the boundary layer to the outer flow is continuous, the "edge" of the boundary layer has been recognized to be the point at which the velocity reaches a certain percentage of the outer velocity, widely accepted as 99% (White 2006, Schlichting et al 2000). At distances farther from this point, the flow of fluid can be approximated as ideal, having no viscosity and no vorticity. Figure 3 illustrates a typical shear layer on a solid surface (Ref 24).

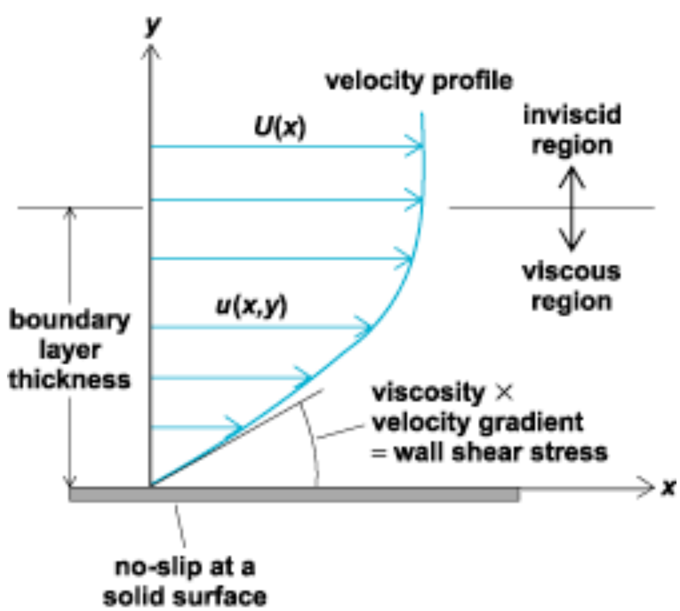

Figure 3. Typical boundary layer velocity profile

At high Reynolds numbers (above 10^6), the inertial forces are quite dominant and the boundary layer remains relatively thin. However, as the Reynolds number decreases and the viscous forces begin to increase relative to the inertial forces, the boundary begins to thicken. A "thin" boundary layer can be approximated when the diffusion time (time required for viscous effects to spread across streamlines) is much smaller than the residence time (time a particle spends near the body), as described by the following equation:

$$\frac{L}{U} \gg \sqrt{\frac{\nu L}{U^3}}$$

With the 9.3" chord model being tested in the water tunnel, the diffusion time is approximately one order smaller than the residence time. Rearranging the equation, we see that this holds true when the Reynolds number is much larger than 1:

$$\sqrt{\frac{UL}{\nu}} = \sqrt{\mathrm{Re}} \gg 1$$

This boundary layer around a curved surface must negotiate areas of favourable and adverse pressure gradients. A favourable pressure gradient is one in which the pressure is decreasing in the direction of the flow and is known to increase the stability of laminar flow. It is present on the leading edge portion of the airfoil where the velocity of the airflow is increasing, thus increasing dynamic pressure and decreasing static pressure. As the curvature of the surface changes sign, the static pressure increases with downstream distance thus creating an adverse pressure gradient – this area is known as the pressure recovery region and is destabilizing to laminar flow. The adverse pressure gradient is accompanied by decreasing flow velocity until a point is reached where portions of the flow very near the surface of the airfoil begin to flow in a direction opposite to that of the free stream. This point is the separation point of the boundary layer (Abbot and Doenhoff 1959, White 2006). At low Reynolds numbers, the freestream laminar flow contains very little kinetic energy to begin with and, in addition to losing energy to the friction forces of the viscous boundary layer, is not able to overcome the adverse pressure gradient and commonly separates before it can transition to turbulent flow.

Boundary Layer Transition and Separation

Depending on the airfoil shape, surface roughness, angle of attack, environmental disturbances and Reynolds number, the separated laminar boundary layer typically transitions to a turbulent flow after separation and will either remain separated or reattach further along the airfoil (Tani 1954, Abbott and Doenhoff 1959, Brendel and Mueller 1987, Mueller and Deslaurier 2003). The area between the laminar separation point and the point of turbulent re-attachment is defined as a laminar separation bubble. The laminar shear layer created immediately following separation is usually unstable and begins at point “S” on Figure 4 (Mueller and Deslaurier 2003). One explanation for the transition process from laminar to turbulent for fully attached flow is the Tollmien-Schlichting process as shown in Figure 5 (White 2006). The Tollmien-Schlichting waves were realized as a solution to the linearized stability equations of Orr-Sommerfeld and ultimately lead to transition to turbulent flow. Transition to turbulent flow of a separated laminar flow typically occurs quickly due the amplification of the aforementioned Tollmien-Schlichting waves and begins at point “T” on Figure 4. The “Dead Air Region” on Figure 4 is characteristic of the separated laminar flow. It is not able to efficiently mix with the free stream and is thus very close to being stationary. If the velocity is near stagnant, so is the pressure gradient and the area therefore corresponds to a pressure plateau. The turbulent flow itself is not self-sustainable. However, one of the significant features of turbulent motion is its momentum exchange with the mean flow thus providing the near wall region with a source of energy from the free stream – indicated by the region of “Reverse Flow Vortex” on Figure 4. This statement results from analysing the Reynolds-averaged Navier-Stokes momentum equation and the continuity equation for the turbulent velocity fluctuations – equations obtained from applying statistical analysis to the theory of turbulence. If enough energy is gained by the turbulent flow, the boundary layer will be able to withstand the adverse pressure gradient and subsequently re-attach.

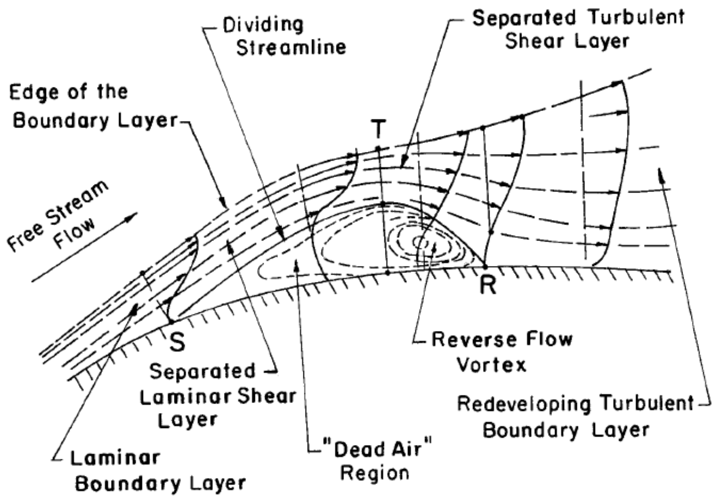

Figure 4. Laminar Separation Bubble Characteristics on an Airfoil (Mueller Deslaurier 2003).

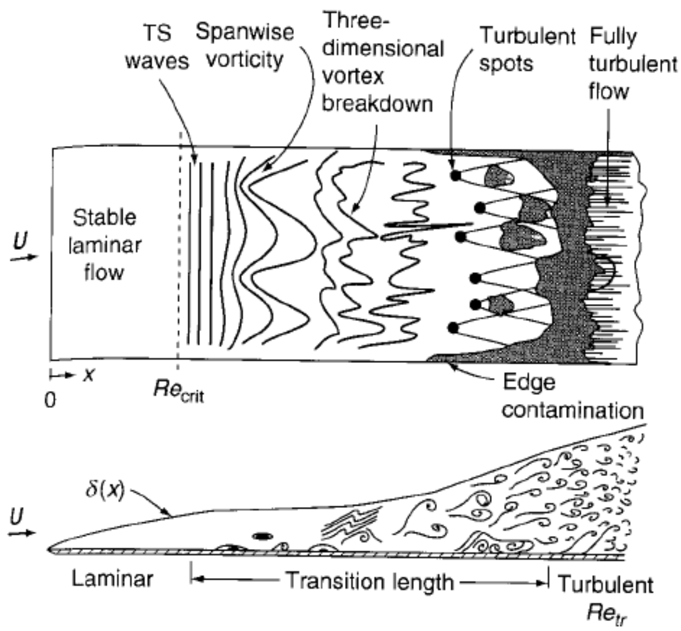

Figure 5. Tollmien-Schlichting Waves Followed by Transition to Turbulent Flow (White 2006).

The location and size of this bubble is also a function of airfoil shape, angle of incidence, environmental disturbances and Reynolds number. (Tani 1954, Abbott and Doenhoff 1959, Mueller and Deslaurier 2003). The difference at high Reynolds number flow is that the unstable laminar boundary layer transitions to a turbulent layer before separating and since turbulent boundary layers contain more kinetic energy than their laminar counterparts, are able to withstand the adverse pressure gradient longer. The velocity gradients of the boundary layer and an illustration of turbulent separation preceded by laminar to turbulent transition is shown is Figure 6 (Talay 1975).

Short and Long Laminar Separation Bubbles

The separation bubble on airfoils has been experimentally shown to exist once the Reynolds number reaches an approximate value of 70 000 and remains as either a "short" or "long" bubble until a Reynolds number of approximately 200 000 (Lissaman 1983) – at which time transition before separation becomes possible. In the lower end of this range, the turbulent flow is not able to entrain enough energy to withstand pressure recovery until quite near the trailing edge of the airfoil and the bubble thus covers about 20-30% of the top surface of the airfoil. Figure 7 (Mueller 1985) is a depiction of a long laminar separation bubble at a small angle of attack. The characteristic pressure plateau is also long, the boundary layer thickness is increased, the lifting forces deteriorate and the pressure drag increases. In the higher end of the Reynolds number range, turbulent reattachment happens rapidly and the pressure gradient is virtually unaffected. This phenomenon will also happen as angle of attack is increased at a fixed Reynolds number. In fact, this short bubble effectively acts as a boundary layer trip and the lift coefficient can increase linearly with angle of attack until stall (massive separation of the laminar boundary layer without reattachment). Figure 8 (Mueller 1985) illustrates a short laminar separation bubble with the turbulent boundary layer separating near the trailing edge. As Reynolds number or angle of attack is increased even further this unstable short bubble may take the shape of a long bubble or separate without reattaching, and it is said to have "burst" (Lissaman 1983, Mueller 1985) – accompanied by the characteristic decrease in lift and increase is drag or stall, respectively. Figure 9 (Mueller 1985) shows the bursting of the short laminar separation bubble which remains detached over a stalled wing. Hysteresis in this process has also been shown experimentally.

Vorticity Dynamics

Because of the relatively sharp leading edge (and associated velocity gradients) of the model chosen for this experiment, there was a significant amount of vorticity generated at the leading edge, which can result in the production of vortices. These vortices entrain energy from the freestream and impart it to the fluid near the surface – the closer the vortices are to the surface, the more energy is gained by the boundary layer. Just as vorticity is convected downstream, so are the structured vortices. Their velocity profile is thus superimposed on the typical velocity profile of the attached boundary layer, a simplified sketch of which is shown in Figure 10.

Flow Control

Controlling the boundary layer flow and ultimately the separation bubble is the next step in improving the aerodynamic performance of low Reynolds number flyers. Many active and passive methods exist, each with their own advantages and disadvantages. This paper investigated the effect of one passive flow control technique - a small diameter circular cylinder and an asymmetric thermocouple wire placed at various locations upstream of the separation bubble. This method of varying the flow characteristics could affect the laminar separation bubble by any of the following ways:

1. If there are vortices being shed from the upstream cylinder and are convected along the upper surface of the airfoil model, they may impart enough energy to the flow near the surface to either reduce or eliminate the separation bubble;
2. The altered flow could trip the laminar boundary layer to turbulence and thus eliminate the separation bubble;

3. Depending on how well the vortex shedding frequencies of the upstream cylinders and the laminar separation bubble are matched could affect the size and possible elimination of the separation bubble; and

4. The modification of the flow field near or at the stagnation streamline changes the curvature of the streamlines near the surface thereby altering the pressure gradient at the surface.

The ability of each of the above-listed characteristics to constructively interfere with the laminar separation bubble and downstream separation point also depends on the location of the wire relative to the leading edge of the model.

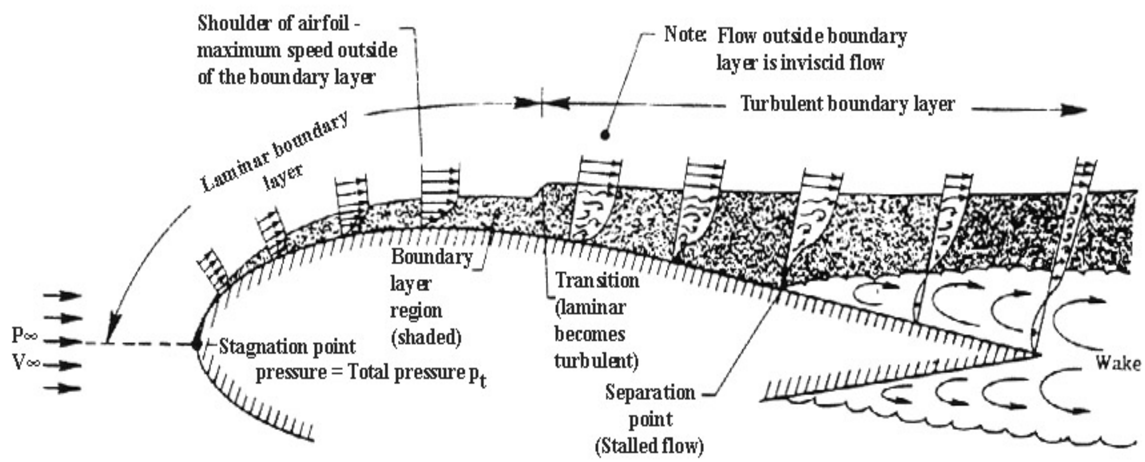

Figure 6. Illustration of Laminar to Turbulent Boundary Layer Transition followed by Turbulent Separation of the Boundary Layer (Talay 1975).

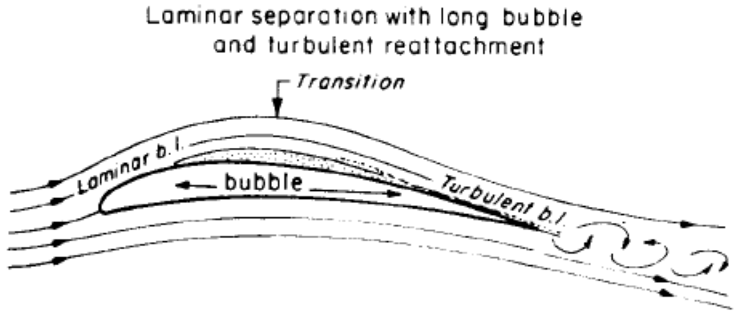

Figure 7. Long Laminar Separation Bubble (Mueller 1985).

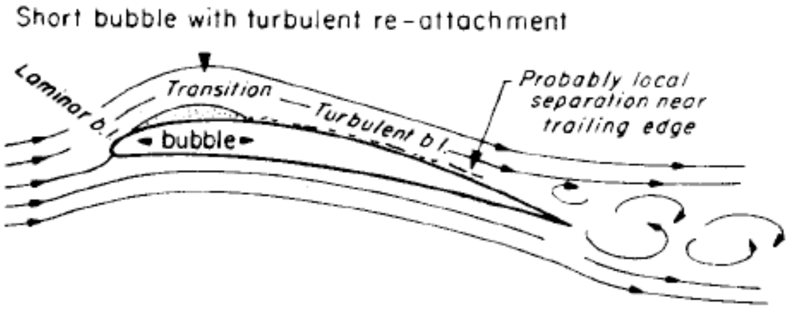

Figure 8. Short Laminar Separation Bubble with Turbulent Separation Downstream (Mueller 1985).

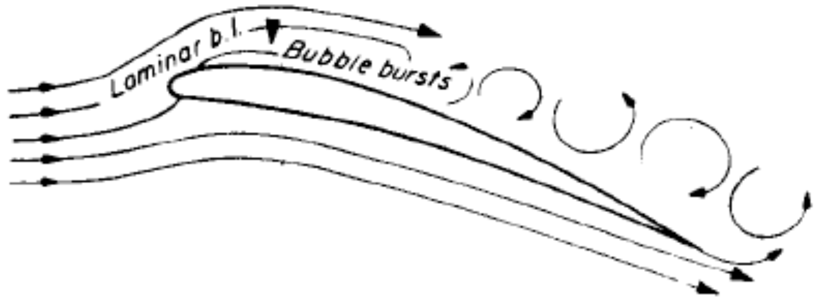

Figure 9. Bursting of the Short Laminar Separation Bubble Without Reattachment (Mueller 1985)

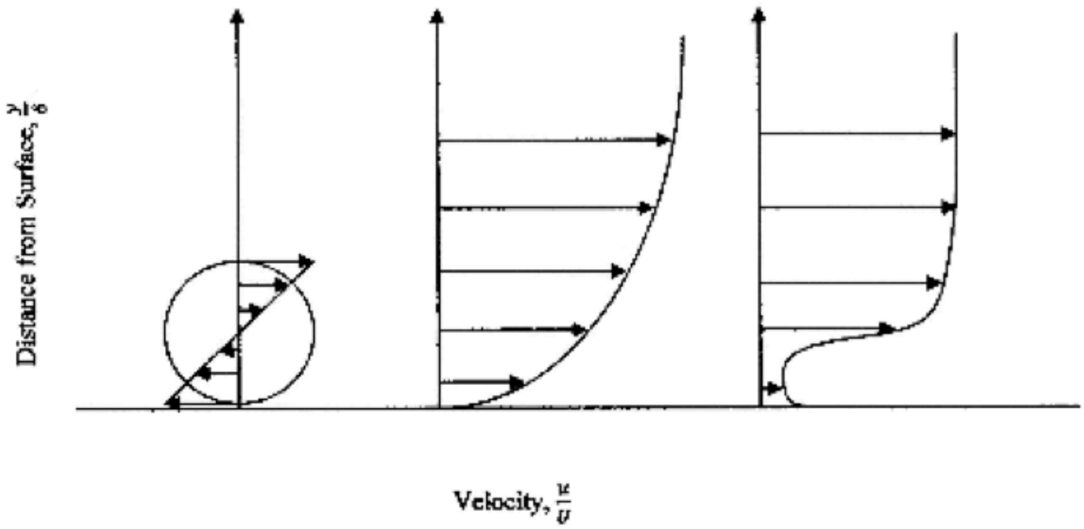

Figure 10. Approximate Sketch of a Vorticity Velocity Profile Superimposed on a Typical Boundary Layer Velocity Profile

Literature Review

In 1969, an article by Tani in 1964 was published in the 5th Volume of Progress in Aeronautical Sciences in which he investigates flows involving the separation bubbles and their effect on stall. Leading edge stall, trailing edge stall, and thin airfoil stall are described along with their effects on the lift curve slope of various airfoils. The presence of the aforementioned stall characteristics are directly related to the presence and type of separation bubbles. The airfoil type and Reynolds number determine whether the bubble is short or long. A short bubble does not significantly alter the pressure distribution over the airfoil but essentially acts as a trip by which the flow transitions to turbulence and reattaches. The long bubble however, is characterized by a large plateau in the pressure gradient and can actually follow the breakdown or "bursting" of the short bubble. He concluded that the presence of the separation bubble "is possible only when the Reynolds number based on boundary layer displacement thickness at separation is greater than a certain critical value". Although useful, this value is not general but is specific to the type of airfoil/object subjected to the flow.

In an Annual Review of Fluid Mechanics in 1983, Lissaman provided a general review of low Reynolds number flow and details on the formation and size of the laminar separation bubble. Like Tani, he concluded that the bubble size significantly impacted the drag and the stall of the airfoil. The size of the bubble itself was noted to be described in terms of a bubble length Reynolds number – generally found to be approximately 50 000. From here he concluded that "for airfoils of chord Reynolds number of about this magnitude, the airfoil is physically too short for reattachment to occur". This also lead to the general observation that the critical Reynolds number based on airfoil chord length is about 70 000. Only above this number could one expect to observe a laminar separation bubble. Without the bubble, the laminar flow would simply separate during the pressure recovery region and fail to re-attach, thus causing a remarkable increase in drag. These concepts are re-affirmed in Mueller's article on "Aerodynamics of Small Vehicles" in the Annual Review of Fluid Mechanics in 2003.

Lin and Pauley (1996) performed a numerical study of the effects of Reynolds number and angle of attack on the laminar separation bubble. They compared their results with low-turbulence wind tunnel tests and found favourable comparison between the two with the limited discrepancies being accounted for by the turbulence in the wind tunnel. They concluded that two dimensional vortex structures shed after laminar separation control the laminar separation bubble and "can be regarded as a reattachment mechanism". Furthermore, they proposed that the limit cycle shedding of the large-scale vortex structures are the primary controlling feature of the bubble and that the "small-scale turbulence plays only a secondary role".

Grundy et al (2001) investigated the effects of acoustic disturbances on low Reynolds number airfoils. Through analysis of previous wind tunnel tests conducted at different facilities and experimentation with varying background noise, he observed that the "acoustic environment appears to be more significant than the turbulence environment" when conducting tests at low Reynolds numbers. In fact, he found that increased background noise aided transition and reduced lift hysteresis.

Separation bubble control was studied by Liu et al (2000) on a Wortman airfoil using the technique of cylinders placed upstream of the airfoil. The diameter of the wire used was defined as 0.25% of the chord length of the airfoil. The wire was tested at various locations upstream and downstream of the airfoil leading edge with the optimum results occurring at the upstream locations. Two wire location positions (x/c, y/c)% = (0.0, -3.2) and (-3.2,-8.0) (measured from the leading edge) resulted in the complete elimination of hysteresis in the lift curve slope and a much gentler stall onset. These results were explained by the possible elimination of the leading edge separation bubble.

Governing Equations

The equations of motion governing laminar boundary layers were first derived by Prandtl in 1904 by applying some boundary layer approximations to the basic equations of motion (Tani 1977). This section will derive and analyse these equations for a two-dimensional, incompressible flow. Figure 11 illustrates the coordinate system over a curved surface (White, 2006).

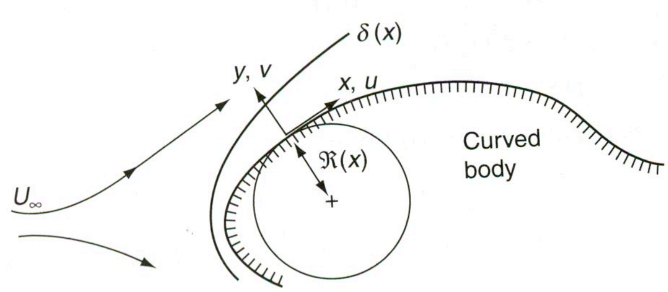

Figure 11. Coordinate System of Boundary Layer Flow (White 2006)

First, the continuity equation is as follows (White 2006):

$$\frac{\partial u}{\partial x} + \frac{\partial v}{\partial y} = 0$$

The Navier-Stokes momentum equations (neglecting buoyancy effects) are (White 2006):

$$\frac{\partial u}{\partial t} + u\frac{\partial u}{\partial x} + v\frac{\partial u}{\partial y} = -\frac{1}{\rho}\frac{\partial p}{\partial x} + \nu\left(\frac{\partial^2 u}{\partial x^2} + \frac{\partial^2 u}{\partial y^2}\right)$$

$$\frac{\partial v}{\partial t} + u\frac{\partial v}{\partial x} + v\frac{\partial v}{\partial y} = -\frac{1}{\rho}\frac{\partial p}{\partial y} + \nu\left(\frac{\partial^2 v}{\partial x^2} + \frac{\partial^2 v}{\partial y^2}\right)$$

To begin the derivation of Prandtl's boundary layer equations from the above, some additional statements regarding the boundary layer must be made. First, the boundary layer must be said to be thin – shown to be true earlier in the present chapter, since the viscous diffusion time is an order smaller than the particle residence time. From this, it can be said that the pressure variation normal to the wall is negligibly small, the velocity component perpendicular to the surface (v) is much smaller than the component parallel (u), and the velocity gradient perpendicular to the wall is much greater than the gradient parallel to the wall (Tani 1977). Theses approximations are shown below (White 2006):

$$\frac{\partial p}{\partial y} \cong 0 \qquad \frac{\partial u}{\partial x} \ll \frac{\partial u}{\partial y} \qquad \frac{\partial v}{\partial x} \ll \frac{\partial v}{\partial y}$$

Since pressure is now a function of x only, Bernoulli's theorem for incompressible flow can be used. Applying these approximations to the Navier-Stokes momentum equation, the dimensional form of Prandtl's boundary layer equations become (White 2006):

$$\frac{\partial u}{\partial x} + \frac{\partial v}{\partial y} = 0$$

$$\frac{\partial u}{\partial t} + u\frac{\partial u}{\partial x} + v\frac{\partial u}{\partial y} \approx \left(\frac{\partial U}{\partial t} + \frac{\partial U}{\partial x}\right) + \nu\frac{\partial^2 u}{\partial y^2}$$

These equations are classified as parabolic – unlike the elliptical nature of their origin, the Navier-Stokes equations. This means that the solution to these equations - the behaviour of the boundary layer – is influenced by both the initial conditions (at x=0) and the boundary conditions. Together with the flat plate integral analysis described below, a significant amount of information can be gained about the laminar boundary layer.

Assuming that viscous forces are much smaller than inertial forces, the boundary layer is laminar and the airfoil can be approximated by a flat-plate, a boundary layer displacement thickness, δ^*, can be calculated by applying the conservation of mass integral equation to a control volume (White 2006). The displacement thickness, as defined below, is valid for incompressible flow, both laminar and turbulent.

$$\delta^* = \int_0^{Y\to\infty}\left(1-\frac{u}{U}\right)dy$$

Similarly, a momentum thickness, θ, can be derived using the momentum integral equation over a control volume and is stated below (White 2006). It can be used to calculate drag in the very limited case of flat plate flow.

$$\theta = \int_0^{Y\to\infty}\frac{u}{U_x}\left(1-\frac{u}{U_x}\right)dy$$

The shape factor is simply a ratio of the displacement and momentum thicknesses and it is always greater than one (White 2006).

$$H = \frac{\delta^*}{\theta}$$

Although the above analysis provides useful information regarding the laminar boundary layer, it does not offer any insight into the conditions required for separation and/or transition to turbulent flow, nor do the equations apply to the turbulent boundary layer.

Analysing turbulent flow requires a statistical approach to solving the Navier-Stokes equation of motion (Tennekes et al 1972). Turbulent velocity and pressure can be decomposed into mean and fluctuating components:

$$u = \tilde{u} + U_t$$

$$p = \tilde{p} + P$$

Inserting these equations into the Navier-Stokes momentum equation gives (Tennekes et al 1972):

$$U_j \frac{\partial U_i}{\partial x_j} + \overline{u_j \frac{\partial u_i}{\partial x_j}} = \frac{1}{\rho} \frac{\partial}{\partial x_j} \mathrm{E}_{ij}$$

The basic continuity equation for turbulent velocity fluctuations becomes:

$$\overline{u_j \frac{\partial u_i}{\partial x_j}} = \frac{\partial}{\partial x_j} \overline{u_i u_j}$$

The term on the right hand side is the mean transport of fluctuating momentum by turbulent velocity fluctuations. Because Newton's second law relates momentum flux to applied forces, the equation above can be interpreted as a stress being applied to the mean flow by the turbulent motion and the momentum equation can be re-written as (Tennekes et al 1972):

$$U_j \frac{\partial U_i}{\partial x_j} = \frac{1}{\rho} \frac{\partial}{\partial x_j} \left(\mathrm{E}_{ij} - \rho \overline{u_i u_j} \right)$$

This equation is known as the Reynolds Momentum Equation and clearly shows the presence of momentum transfer between the turbulent and mean flow thus preventing the decay of turbulence which later leads to reattachment of the boundary layer. Exactly how and when this happens is essentially the closure problem of the study of turbulence – more variables than existing equations. Although many methods exist to bridge this gap, their details are beyond the scope of this study.

Chapter 3

EXPERIMENTAL APPROACH

Introduction

Low Reynolds number flow is extremely vulnerable to free stream disturbances (Donavan and Selig 1989, Adrian 1996) and it is therefore crucial to limit experimental methods that interfere with the flow. Besides finding a non-intrusive method of experimentation, any measuring device used must be capable of sensing very small changes in aerodynamic forces. The size of the airfoil itself presents challenges in accurate construction as well as installation of any force measurement device – i.e. pressure taps or a force balance system. The experimental methods of choice were thus flow visualization in the water tunnel through dye injection, and qualitative velocity measurements of the boundary layer downstream of the separation bubble using hot-film anemometry.

Water Tunnel

The UTSI water tunnel can be more appropriately referred to as a water channel system. It is a closed circuit, continuous flow horizontal configuration with a free surface driven by a 4 blade bronze propeller in a 12 inch pipe joining the upstream and downstream tanks. The test section has a width of 15 inches, length of 60 inches and a maximum water depth of 18.125 inches (although limited to 16.75 inches by the current filtration and drainage systems). The free top surface of the water tunnel provides easy installation of and access to the model and the remaining three surfaces of the test section are clear Plexiglas for ease of viewing. Combining these features with the ability to reproduce low Reynolds number flows, the water tunnel is therefore an appropriate facility for this investigation.

Although the water tunnel can achieve a water velocity of three feet per second, previous studies involving the water tunnel noted the presence of a standing wave at the higher velocities (Michalchuk 2006). A standing wave would introduce a disturbance highly undesirable for investigating separation bubble characteristics at low Reynolds numbers. The maximum functional water velocity for these tests was thus decided to be one foot per second. Additionally, hydraulic jam was observed in preliminary experimental tests during this project when the model was suspended at an angle of attack of 22 degrees.

To ensure the dye used for flow visualization accurately reflects the dynamics of the flow, its density must be matched to the fluid density in which it is flowing (in addition to providing color contrast for detailed visualization). The recipe for the dye used in this investigation included a mix of tap water, Polyethylene Oxide, fluorescent particles and denatured alcohol. Care must also be taken to ensure the dye is injected into the boundary layer in a manner as least disruptive to the flow as possible. As shown in Figure 12, a piece of tubing was attached to the dye probe behind the model, followed the contour underneath the model and was then fastened in a location such that the dye entered the flow at the leading edge of the model. The dye was fed under pressure to the dye probe and tubing through pressured canisters shown in Figure 13.

Model

A section of PVC tubing was chosen as the medium by which to examine the separation bubble. The size was chosen to create flows dynamically similar to the flight of the MAV – i.e. matching the Reynolds number. In addition, the shape of the model is compatible with some current deployable, folding wing MAVs. The leading edge radius was relatively small due to the machining and PVC material. In real applications, different profile airfoils could be used for laminar flow application. Given the functional velocity range of the water tunnel and the availability of PVC tubing, the choice was made to use a section of 16 inch diameter tubing to yield a model with a chord length of 9.33 inches and height of 1.5 inches. The upper surface of the PVC tube was finely sanded, smoothed and painted with high gloss paint to reduce surface roughness. Black paint was chosen to help visualize the flow characteristics as portrayed by the fluorescent dye.

The model was mounted between two Plexiglas endplates to reduce span wise fluid flow and to help ensure two dimensional flow at the location of the light sheet. Angled gridlines in increments of two degrees were marked on the right endplate as seen in Figure 12. When matched with a horizontal grid attached to the outside of the water tunnel test section (also seen in Figure 12), these gridlines provided the angle of attack of the airfoil model. Figure 12 is a two dimensional view of the model, the endplates and the mounting mechanism described later in this section. Detailed drawings of the model and endplates are presented at Appendix A.

Additionally, the drawings at Appendix A show the matching holes at specified locations on the endplates through which the wires were fed to be placed in the upstream flow of the model. The location of the wire is referred to by it's row and column number as demonstrated in Figure 15. The first wire used in this experiment was a circular cylindrical shape with a diameter of 0.01". The second wire used was a piece of thermocouple extension wire with dimensions as shown in Figure 16. When secured to the endplates, the thermocouple wire was oriented such that the largest surface (height of 0.07 inches) was perpendicular to the flow and the effective chord was 0.045 inches. Both wires are pictured together for visual comparison in Figure 17 and Table 1 lists the Reynolds numbers of these cylinders for each of the chord Reynolds numbers analysed. The model and endplate configuration was mounted to a traversing sting support system in place on the top rails of the water tunnel that allowed movement in five degrees of freedom: linear motion in the x, y and z axis as well as rotational motion about the x and y axis. The only degree of freedom that was varied for this experiment was the rotational motion about the y-axis (angle of attack), all others remained fixed. Figure 18 illustrates the model mounted on the traversing support system in the water tunnel test section.

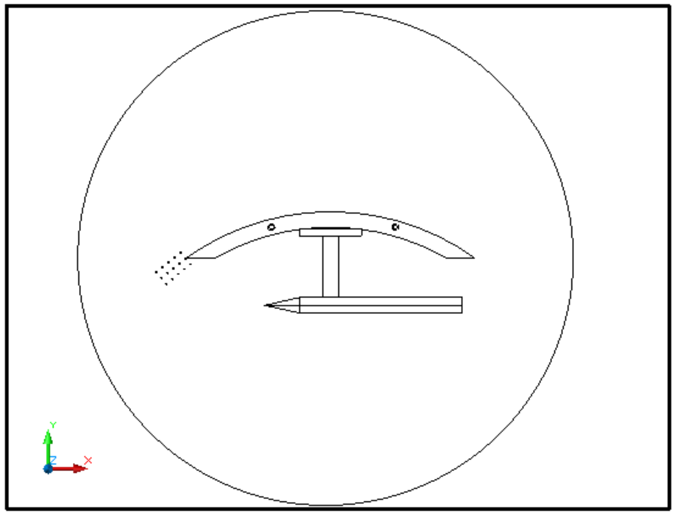

a. Two Dimensional AutoCAD Drawings

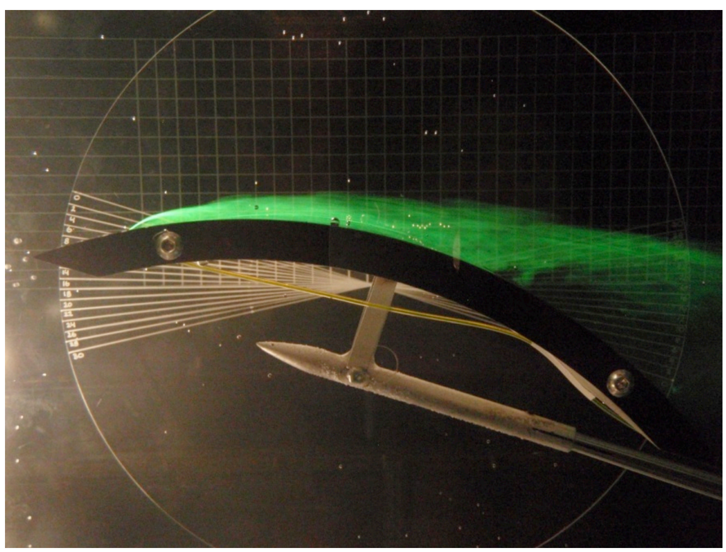

b. Two Dimensional Image (only the right endplate is visible)

Figure 12. Two Dimensional View of Model With Endplates and Mounting Mechanism

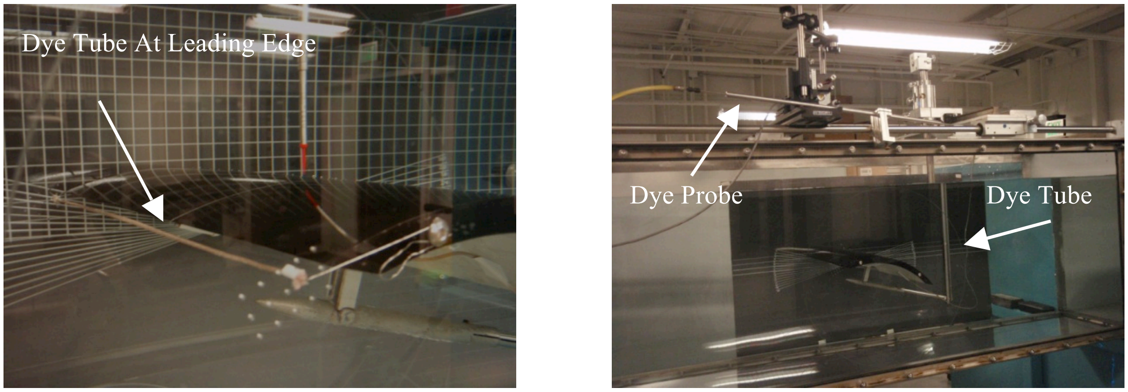

Figure 13. Dye Tube and Probe Placement

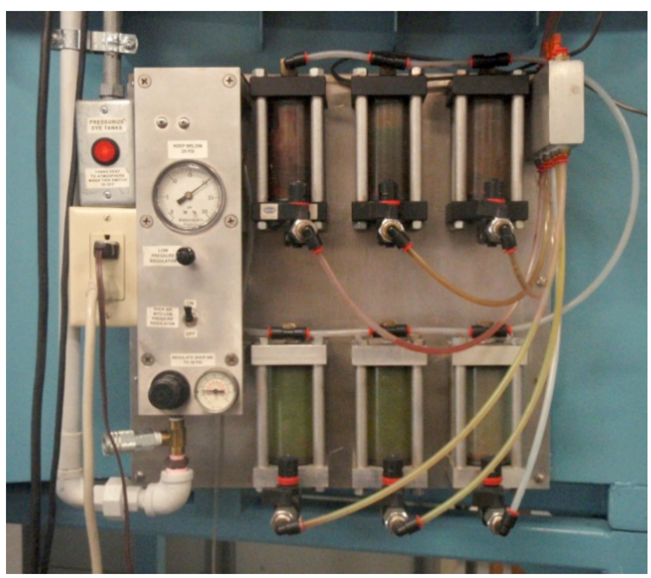

Figure 14. Pressurized Dye Canisters

Table 1. Reynolds Numbers Based on Small Cylinder Wire Diameters

Model Chord Reynolds Number (Re_c)	Reynolds Number of 0.01 inch Diameter Cylinder (Re_{d1})	Reynolds Number of 0.045 inch Diameter Cylinder (Re_{d2})
27,000	29	132
45,000	49	218

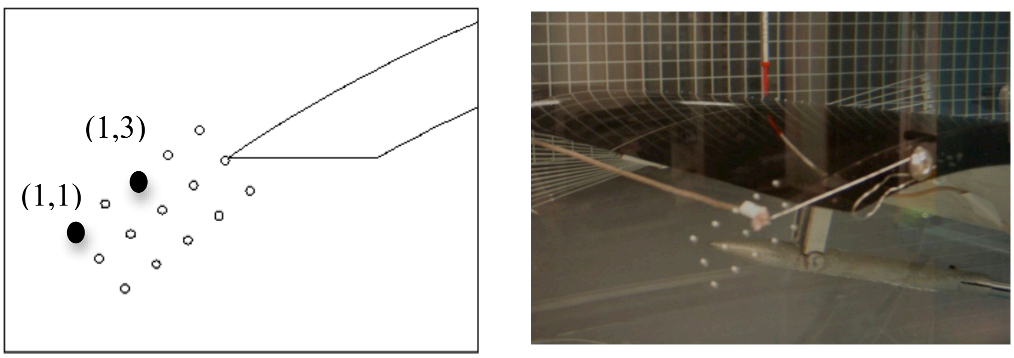

Figure 15. Wire Location Coordinates

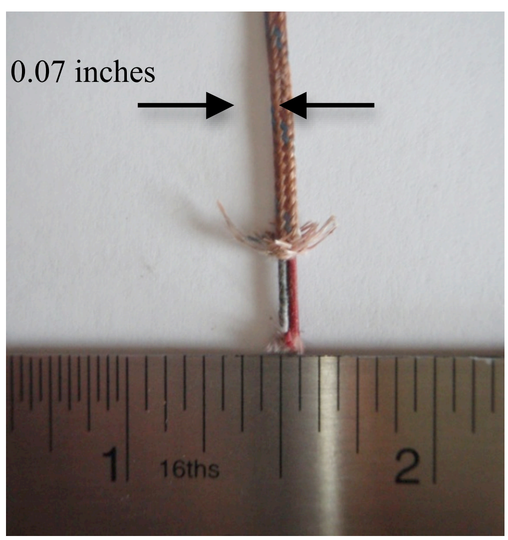

Figure 16. Thermocouple Wire

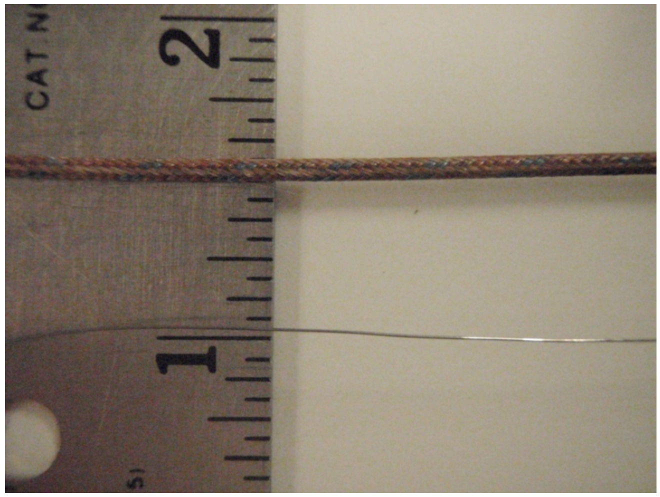

Figure 17. Comparison of Cylindrical Wire and Thermocouple Wire

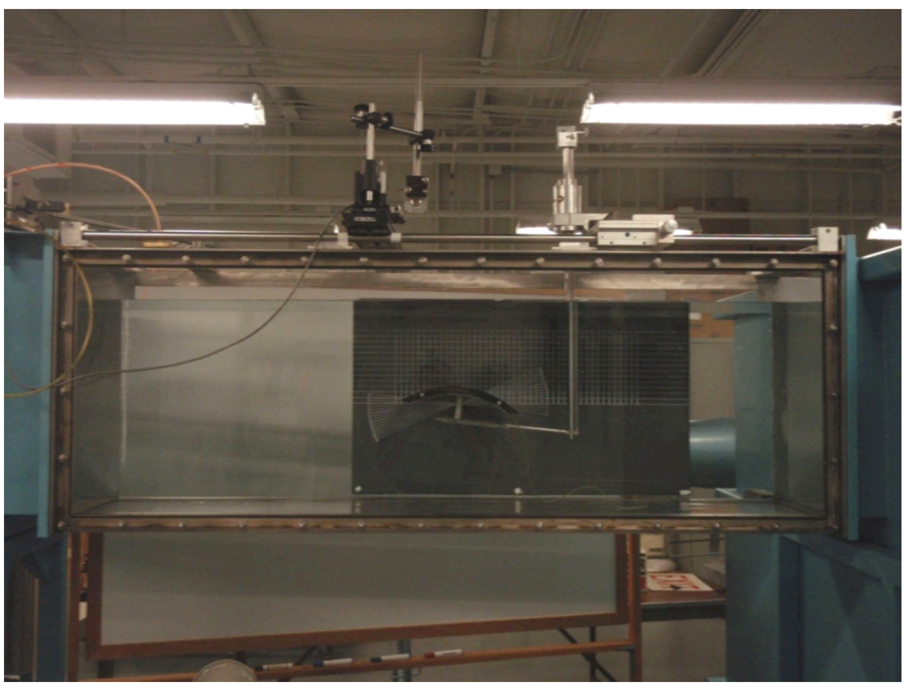

Figure 18. Model Mounted on Traverse in Water Tunnel Test Section

Flow Visualization

A 4 milliwatt laser beam with a wavelength of 500 nanometers was directed through a scanner with six rotating mirrors to produce a vertical light sheet over the model at the y-location at which the dye was entering the flow. The fluorescent dye was thus illuminated to produce a two dimensional view of the fluid dynamics as it negotiated the curvature of the model. Figure 19 illustrates the details of the set-up of the laser and scanner. Figures 20 and 21 show detailed pictures of the laser and scanner.

Photographs of the leading edge separation bubble and the downstream separation point were taken with an Olympus E-10 digital camera. This camera was chosen as the most suitable because it had the option to manually focus and to make simultaneous manual selections of the aperture value and shutter speed.

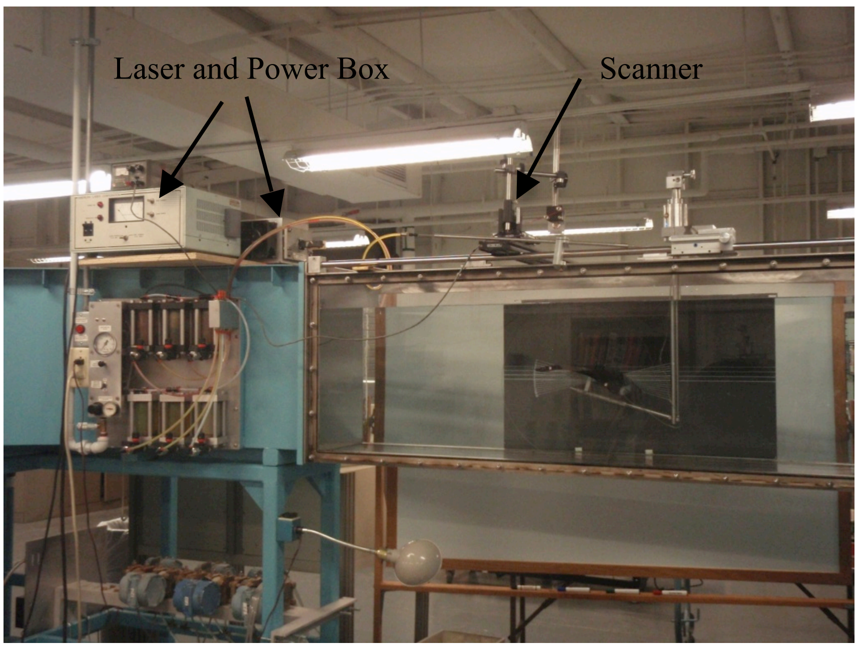

Figure 19. Set-up of Laser and Scanner

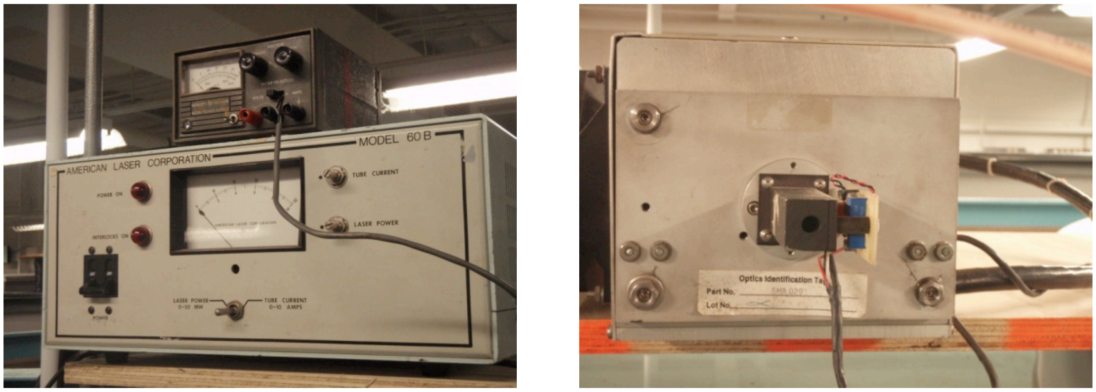

Figure 20. Details of Laser

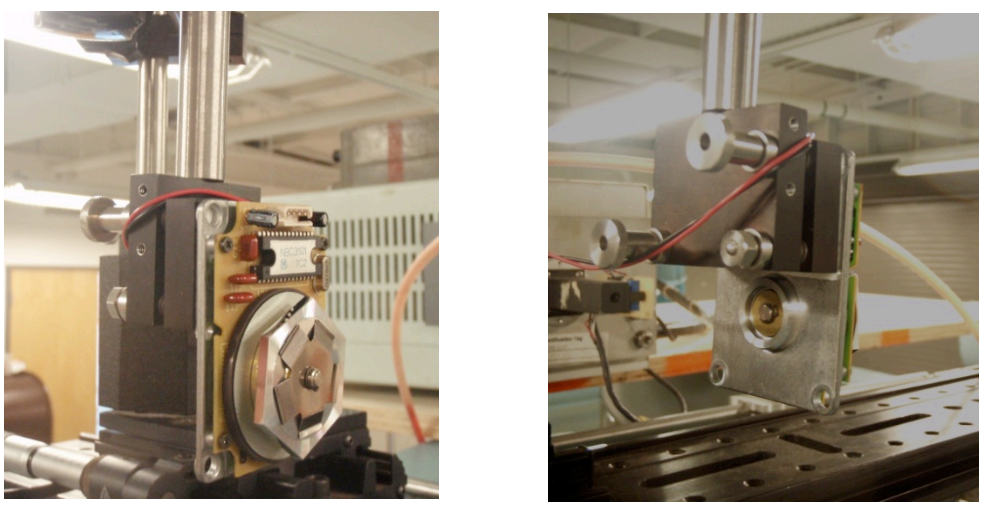

Figure 21. Details of Scanner

After systematic testing, the best camera settings to capture the details of the separation bubble and the downstream separation point were identified and are listed in Table 2.

While operating the camera under the settings listed above, the exposure level was automatically adjusted by the camera. The photographs were then batch processed using the Image Processing Toolbox in MATLAB version R2009a. To clearly view the details of the leading edge separation bubble, the images were first cropped, then filtered and colour segmented. The type of filter used was the “motion” type which approximates linear horizontal motion. The cropped and filtered image was then converted to L*a*b colour space and segmented into three clusters based on the colour information contained in the “a” and “b” layers. To clearly view the average downstream separation point from the photographs taken at a relatively long shutter speed, the images were cropped and filtered using several different filters for maximum clarity. The filters used were the “motion” filter as described above, in addition to an averaging filter and a contrast enhancement filter. The MATLAB code for both image processing schemes are found at Appendix C.

Using the “imtool” function in MATLAB, each image was closely analysed and measured. The arc length of each bubble was measured by counting the pixels between the boundary layer separation point at the leading edge and the reattachment point. The pixels per inch in the image was calculated using an image of the background grid taken with the same camera settings. The height of the separation bubbles and the arc length between the leading edge of the model and the downstream separation point were calculated in the same manner.

Table 2. Camera Settings to Capture Details of Laminar Separation Bubble and Downstream Separation Point

Setting	Leading Edge Separation Bubble Pictures	Downstream Separation Point Pictures
ISO	320	320
Shutter Speed	100	2.0
Aperture Value	2.4	2.2
Resolution	2240 x 1680 pixels	2240 x 1680 pixels
Zoom	Maximum TELE	Maximum Wide
Sharpness	High	High
Contrast	High	High

Hot Film Anemometry

A constant temperature anemometer was used to gather quantitative velocity data in the boundary layer downstream of the separation bubble. To reduce interference effects on the bubble and to remain in the attached boundary layer, it was decided to test the boundary layer velocity profile at two locations on the model: x/c=0.12 and x/c=0.25. The sensor used in this experiment was a TSI™ 1210-20W hot film sensor for use in water, serial number 924203 shown in Figure 22. It was a solid quartz cylinder coated with a very thin layer of platinum over which is a coating of electrically insulating quartz. Both the calibration of the sensor and the acquisition of velocity measurements were performed using the IFA 300 anemometer and a personal computer.

The calibration of the sensor was completed in a water tow tank as pictured in Figure 23. A variable speed motor pushed the mounted sensor through a four foot section of the tow tank at known velocities and the IFA 300 anemometer computed the calibration. The gain and offset were calculated to maximize the range of the anemometer. The calibration details along with the calibration curve can be found at Appendix D.

The sampling rate of the hot film data was 40,000 Hertz for one second intervals. The values shown in this report are an average value of the samples.

A fabricated "stop" was attached to the anemometer probe to fix the y location of the first data point. The attachment point to the probe was marked to provide repeatability of this first point. Figure 22 portraying the hot film sensor used in this experiment includes the stop as attached to the probe and sensor. This apparatus was then secured to a mount on top of the water tunnel that allowed y-direction movements in increments as small as 0.1 millimeters. Figure 24 portrays the model and hot-film sensor set-up.

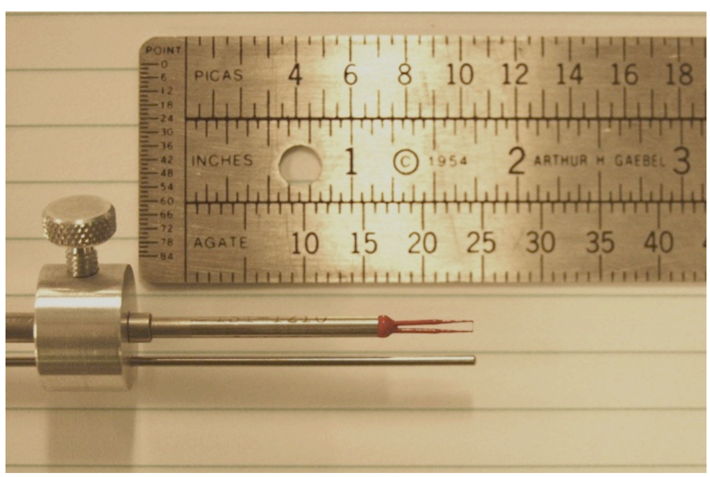

Figure 22. Hot Film Sensor and Fabricated "Stop"

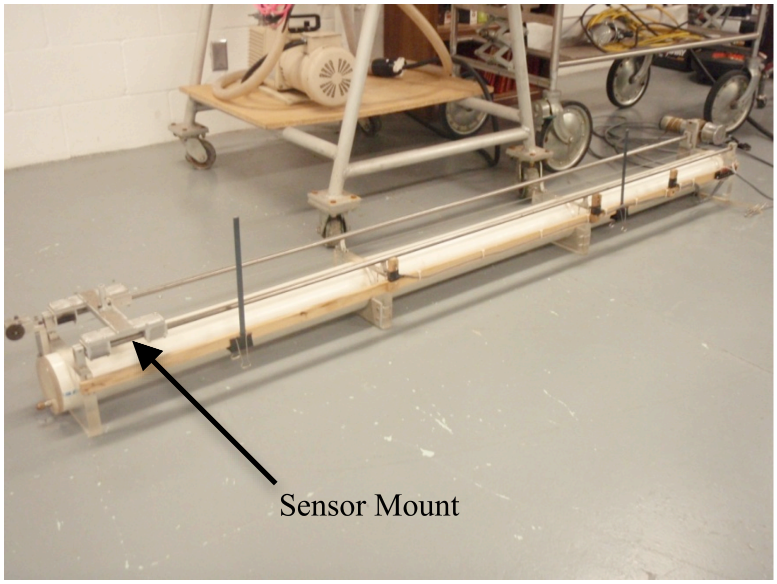

Figure 23. Hot Film Sensor Calibration Tow Tank

Figure 24. Model Set-up For Hot-Film Velocity Measurements

Test Variables

The Reynolds numbers at which the tests were conducted were chosen to imitate the range at which the MAVs would operate and by the functional capability of the water tunnel system in place at UTSI. Preliminary testing showed that Reynolds number of 27,000 and 45,000 met the criteria mentioned above and were sufficiently different to produce noticeable changes in both the laminar separation bubble and the downstream boundary layer separation point.

The angles of attack that were chosen to be included in this study were 14, 16 and 18. They were chosen because they sustained a laminar separation bubble at the Reynolds numbers of interest, there was no risk of hydraulic jam in the water tunnel, and there was generally a clear re-attachment point of the separation bubble and thus the clarity at which images of the separation bubble could be captured was the greatest. Preliminary tests indicated that the bubble began to form when the model was at an angle of attack of 12 degrees but was not sustained over a wide range of Reynolds numbers. As mentioned previously, hydraulic jam was visually noticeable at an angle of attack of 28 degrees and beyond 20 degrees, the re-attachment point of the laminar separation bubble could not be easily identified.

Preliminary testing with various sized cylindrical wires placed upstream of the leading edge indicated that good results may be acquired with wires of diameter 0.01 inches or greater. It was therefore decided to use a cylindrical wire of diameter 0.01 inches and a piece of thermocouple wire with a 0.045 inch surface perpendicular to the freestream. The wire locations that showed the most potential were (1,2), (1,3), (2,3), (2,4), (2,5), (3,2), (3,3), and (3,4).

Chapter 4

EXPERIMENTAL RESULTS AND ANALYSIS

All Figures referenced in this chapter are found in Appendix D of this paper. Figures 29 and 30 are sample images showing how the bubble length, bubble height and separation point were measured. Since the model was painted with high gloss black paint, the images in Appendix D show a great deal of reflection in the model. Figure 29 illustrates the line of symmetry in the image which is the actual contour of the model thus differentiating between the flow characteristics and their reflection.

Flow Visualization

Baseline Configuration

The configuration referred to as the "baseline" is the model with no wire installed upstream of the leading edge. This is the configuration to which all subsequent tests were compared. The images captured with the model in the baseline configuration themselves provide a great deal of insight into the leading edge laminar separation bubble. First, the boundary layer is separating from the leading edge and reattaching in the region of decreasing pressure – i.e. favourable pressure gradient. At an angle of attack of 14 degrees and Reynolds number of 27,000, shown in Figure 31, there is a distinct region of re-circulating fluid with a clear boundary (at which exists a shear layer), followed by a relatively intense vortex at the point of reattachment. This vortex is very close to the surface of the model and is thus able to impart a great deal of energy from the mean flow to the near-wall region. This entrainment, combined with the favourable pressure gradient and the dominance of the shear layer over the region of "dead fluid" enables the boundary layer to reattach quickly to form a short leading edge bubble. After reattachment, the fluid flow appears to be very smooth and orderly with vortex structures being stretched as they are convected downstream. The images at the higher angles of attack (16 and 18 degrees) portray different flow characteristics than the image of the model at 14 degrees. There is still a clearly bounded region of re-circulating fluid, but the vortex structure near the bubble re-attachment point is farther away from the surface of the model and is thus not able to impart as much energy to the near-wall region. The exact re-attachment point becomes less obvious and the measurement of the bubble length less precise – in fact the difference in the average bubble length at 16 and 18 degrees is within the calculated error band. The boundary layer does appear however, to reattach a little farther downstream than that at a 14 degree angle of attack, owing to the decreased impact of the vortex combined with less of a favourable pressure gradient. The shed vortex structures are less defined and are diffused into large, apparently turbulent regions containing smaller, random turbulent eddies – possibly indicating the presence of the cascading effect. Figure 32 displays the images of the leading edge fluid flow at a Reynolds number of 45,000. There is a noticeable decrease in separation bubble length with an increase in Reynolds number owing to the increased velocity (and kinetic energy) of the mean flow producing a steeper gradient in the shear layer thus enabling the boundary layer to re-attach quicker. Although there are defined vortices present at the separation bubble boundary, they are relatively far from the surface resulting in less entrainment of the mean flow energy. As the angle of attack increases at this higher Reynolds number, it appears that, as the large scale vortices are convected, they become larger, less defined and more diffused. All three images are exhibiting signs of the smaller random turbulent eddies. In the image of the model at an angle of attack of 18 degrees, there does not appear to be a clear reattachment point, resulting in a larger error band in the bubble length measurements. A consistent increase in bubble thickness is noted with an increase in angle of attack at both Reynolds numbers due to the increase in boundary layer separation angle. Graphical representations of the separation bubble length and bubble thickness are displayed in Figures 33 and 34. The x-location of the re-attachment point is non-dimensionalized by the chord length of the model and the thickness is non-dimensionalized by the boundary layer thickness calculated using the hot film velocity measurements at $x/c=0.18$.

In addition to the observations discussed above regarding the leading edge flow characteristics, there is also some information to be gained through analysis of the global, slower shutter speed pictures depicting the average downstream separation point. At a Reynolds number of 27,000, there is a noticeable increase in the downstream separation point between the model at an angle of attack of 14 degrees and the two higher angles. This could be explained by the difference between a laminar boundary layer separation and turbulent boundary layer separation – the latter having more energy to withstand the adverse pressure gradient experienced along the back half of the model. Figures 35 and 36 portray the images of the downstream separation location at the three angles of attack, and Figure 37 is a quantitative comparison of the non-dimensionalized measurements of this location. In the images, it is clear that as the angle of attack is increased, the dye becomes more diffused and less concentrated making the separation point increasingly more difficult to pinpoint. The situation is made worse by the fluid being re-circulated in the separated region masking the departure of the visible streaklines from the model. At the higher Reynolds number, there is negligible difference in the separation point between each of the images at the three angles of attack.

Cylindrical Wire Impact

The impact the 0.01" cylindrical wire had on the separation bubble and downstream separation point was minimal, the only noticeable effects occurring when the wire was placed at locations (2,3) and (2,5). Given this minimal impact and the Reynolds numbers based on the diameter of the cylinder (29 and 49), it is unlikely that any vortices were shed from this upstream cylinder, leaving small fluid oscillations from the cylinder, the streamline alteration and possible small scale turbulence to account for the small changes in the separation bubble. For each angle of attack at the lower Reynolds number, the bubble was slightly reduced in length and height with the exception of an 18 degree angle of attack at a Reynolds number of 27,000 at which test point the delta was within the error band. At the higher Reynolds number, the separation bubble seemed to slightly increase in length at all angles of attack, although the location of the specific reattachment point was not easily detectable and the average lengths were within the outer ranges of the error band. The noticed interference in this case can be explained by the increased frequency and size of oscillations from the circular cylinder as it's Reynolds number based on diameter was increased accordingly. Despite the small changes in the separation bubble, there were negligible changes in the shedding vortex characteristics and the downstream separation point. Figures 38 and 39 are a sample of images of the separation bubble at an angle of attack of 14 degrees and both Reynolds numbers illustrating the slight degree to which the fluid was impacted by the upstream wire. Graphical representations of the bubble length and separation point locations versus angle of attack for both Reynolds number are found in Figures 40 through 43.

Thermocouple Wire Impact

Unlike the cylindrical wire, the flow variation caused by an upstream thermocouple wire had a significant impact on the laminar separation bubble and the downstream separation point – consistent with the fact that vortices were very likely shed from the cylinder given the Reynolds numbers (132 and 218) resulting in a possible increase in energy in the flow near the surface at the leading edge depending on the wire location. When placed at the locations of (1,2), (2,3) and (2,4) the presence of the thermocouple either nearly or completely eliminated the separation bubble leaving leading edge vortices with varying behavioural characteristics. Figures 44, 45, and 46 illustrate the flow at the leading of the model at a Reynolds number of 27,000 and an angle of attack of 14, 16 and 18 degrees respectfully while Figures 47, 48, and 49 show the corresponding downstream separation point. Similarly, Figures 50, 51, and 52 illustrate the leading edge flow at a Reynolds number of 45,000 and Figures 53, 54, and 55 portray the downstream separation point at this Reynolds number.

With the thermocouple wire placed at (1,2) at a Reynolds number of 27,000, an extremely small area of possible re-circulation is present although the re-circulation itself was not visibly seen during the experiment. Immediately following this region is a large, well-organized vortex capable of entraining mean flow energy to the near-wall region of fluid – again, an indication of how much vorticity is generated at the leading edge of the model. However, the shed vortices appear to be diffused very quickly as they are convected downstream, possibly decreasing the exchange of energy due to the angular velocity of the vortex. Due to the efficient momentum exchanging capabilities of turbulent fluid, these possibly turbulent regions of diffused vortices may also be able to impart momentum into the boundary layer. As angle of attack is increased, the shed vortices diffuse into regions of increasing size and eventually merge together. The thickness of the possible separation bubble at the leading edge also increases, as expected with increased angle of attack. With an increase in Reynolds number, the first visible vortex appears smaller and farther away from the surface of the model (consistent with more concentrated vorticity at higher Reynolds numbers), leaving only the steeper velocity gradient of the shear layer to initiate re-attachment of the bubble and the momentum exchange of the possible turbulent regions to impart energy to the boundary layer. Additionally, the small separation bubble appears to slightly decrease only in length with negligible changes in height with the increased Reynolds number.

Despite the drastic reduction in the region of re-circulating fluid at the leading edge, the changes in downstream separation point between the baseline configuration and the thermocouple wire configuration were not detectable with the exception of an 18 degree angle of attack. At both Reynolds numbers, graphically presented at Figures 56 and 57, the boundary layer appeared to separate from the surface further upstream than the baseline configuration. This is the result typically expected as angle of attack is increased because the adverse pressure gradient begins further upstream and is more severe. At a higher angle of attack, the images also show the vortices generated near the leading edge to be farther from the surface of the model and therefore not able to impart as much energy into the region near the surface and ultimately the boundary layer.

When the thermocouple wire was placed at (2,3), the laminar separation bubble appeared to be completely eliminated when the model was angled at 14 and 16 degrees at the lower Reynolds number and at all angles of attack at the higher Reynolds number. At an angle of attack of 14 degrees and both Reynolds numbers, a unique vortex characteristic presented itself. There appeared to be two well-defined large vortices being shed very close to each other thus influencing the velocity field that typically surrounds a vortex enabling the entrainment of energy. Because of this influence, the maximum amount of benefit seen by boundary layer decreases and the expected level of energy in the boundary layer correspondingly decreases. Although difficult to tell in the image at the higher Reynolds number, there is possibility of vortex pairing as the two vortices are being convected downstream as indicated by the merging regions of the diffusing vortices. At angles of 16 and 18 degrees at the lower Reynolds, the vortices generated at the leading edge appear larger and spaced farther apart than those at an angle of 14 degrees. As the vortices are convected downstream, they appear to diffuse into larger regions of possible turbulent flow with some indication of the presence of random eddies. As the angle increased, the structures became less defined. As the Reynolds number was increased, the structures appeared smaller, more diffused and less structured.

Similar to the case in which the flow was altered by the thermocouple wire placed at (1,2), the change in downstream separation point was only significant (greater than the error band) at an angle of attack of 18 degrees at both Reynolds numbers – this change being an upstream movement in the separation point. Again, this result indicates that the fluid near the surface of the model did not contain as much energy as that in the baseline configuration with which to overcome the larger, steeper adverse pressure gradient region of the higher angle of attack. One contributing factor can again be the fact that the well-defined vortices near the leading edge moved farther away from the surface of the model with angle of attack.

When the leading edge flow was modified by the thermocouple wire placed at (2,4), the visible vortices formed closer to the leading edge than all other cases leaving no area of possible re-circulation. This phenomenon held true for all angles of attack and all Reynolds numbers. At an angle of attack of 14 degrees, the vortices also remained more structured and defined significantly longer as they were convected downstream along the surface. The degree of definition of these vortices at this configuration indicates that the frequency and phase of the shedding vortices from the upstream cylinder were closely matched to those of the leading edge vortices – the ideal situation of constructive interference by the upstream cylinder. This could translate to more energy being entrained by the vortex from the mean flow to the region near the surface and the boundary layer. As the angle of attack increased, the vortex nearest the leading edge was formed farther from the surface thus inhibiting it's ability to transfer energy. Also with an increase in angle of attack came more diffusion of the vortices into larger regions that eventually seemed to merge at an angle of attack of 18 degrees and the higher Reynolds number. As previously discussed in the preceding configurations, the more diffused the vortices, the more indication of the cascading of large structures into smaller random turbulent structures.

At an angle of attack of 18 degrees at the lower Reynolds number, Figure 52 indicates that there was not a significant change in the average downstream separation point as with the previously discussed cases indicating that the fluid contained more energy. However, the error band associated with this measurement was large enough to include the measurements of the baseline configuration as well as the cases with the thermocouple wire placed at (1,2) and (2,3). The large range of measurements could indicate periodicity of the separation point that is further impeded by the increase in noted diffusion at that angle of attack. The change in separation point at all other angles of attack and Reynolds numbers was not outside the calculated error band and thus considered negligible.

Error Analysis

Several sources of error must be taken into consideration when analysing the images discussed above. First, the velocity measurements with which the Reynolds numbers were calculated contained enough of a spread that the repeatability of the Reynolds numbers was within approximately 6% translating to a bubble length spread of x/c=0.001. Next, the largest change in bubble length with a two degree angle of attack was measured to be x/c=0.007 or a delta of 0.0035 per angle of attack. The angle of attack was marked in increments of 2 degrees on the endplates attached to the model (they were not removed from the model for the duration of the experiment) at such a radius as to clearly distinguish a change of least one half of a degree. This would correspond to a bubble length spread of x/c=0.001. The spread calculated from these two factors was added to the spread calculated from measuring the four images of the same configuration (taken seconds apart) to result in the plus or minus measurements listed in the figures and graphs. Contributing to the difference in measurements taken from theoretically identical images were the periodic nature of both the laminar separation bubble and downstream separation point, the phase of the shedding vortices, the diffusion of dye both near the re-attachment point of the separation bubble and the downstream separation point and the re-circulating fluid in the separated region just downstream of the separation point. The factors that were considered to contribute negligible error were: the camera zoom since it was operated at either max "tele" or max "wide" every time for the bubble and separation point images; the camera location since the tripod legs were placed on markings on the floor and were moved as little as required; and the location of the model in the test section since the model was marked so that the laser was illuminating at the same z-location each time.

Hot Film Anemometry Velocity Measurements

Hot film anemometry measurements of the boundary layer velocity profile were conducted at two locations on three model configurations at a Reynolds number of 27,000. The configurations were: the baseline for comparison purposes, and; thermocouple wires placed at (2,3) and (2,4) since they appeared to have the most impact on the fluid flowing over the model. The locations were chosen to avoid disturbing the separation bubble and to remain within the attached boundary layer. These two locations were x/c=0.12 and x/c=0.25 (non-dimensionalized by the model chord length). The y locations of the measurement points were non-dimensionalized by the boundary layer thickness estimated for that configuration.

Table 3 lists the approximated boundary layer thickness for all measurement locations and angles of attack. In all cases except one, the boundary layer thickened with an increase in angle of attack. The exception occurred with a thermocouple wire placed at (2,3) at the downstream measurement location. Upon inspection of the images in Figure 47, the dye appears more intense and concentrated possibly indicating a more orderly flow at that location than the other configurations – explaining the apparent thinner boundary layer. However, there does not appear to be a significant difference between the images at angle of attack of 14 and 16 degrees indicating an experimental error may be present. Either the velocity was not measured at sufficient distance from the surface or the location of the starting point was erroneous.

Figures 58 and 59 illustrate the velocity profiles at the x/c=0.12 and x/c=0.25 locations respectfully, at an angle of attack of 14 degrees for all three configurations. Although some scatter is present in the data, a clear trend is visible for all three profiles. In each case, but more dominant in the baseline and thermocouple wire at (2,3) configurations, the influence of the vortex velocity profile is evident. Whether or not this trend appears and the reason for some scatter at the locations closer to the model is due to the phase of the vortex shedding. The gradient appears to be less steep at the location further downstream, indicative of the turbulent regions forming as the fluid is convected downstream along the surface of the model.

Figures 60 and 61 show the velocity profiles at the x/c=0.12 and x/c=0.25 locations respectfully, at an angle of attack of 16 degrees for all three configurations. The scatter in all cases seems to increase, consistent with the increased vortex diffusion and likely presence of random turbulent eddies at that angle of attack. Additionally, although difficult to depict, the velocity gradient does not seem to change between the two measurement locations, again consistent with increased diffusion and random eddies as noted in the analysis of the associated images in the previous section.

Error Analysis

At zero velocity, the sensor itself is generating a small velocity due to the natural convection of heat from the wire. This velocity it estimated at 10 millimeters per second for the hot film sensors used in water (Ref 27). If the fluid being tested is at low velocities, this error would be remain closer to this maximum value than if testing was occurring at higher velocities. Additionally, for any given test condition the precision at which the measurements were taken was found to be approximately 6%. Although the location of the fabricated "stop" was marked so that it could be placed at the same location for the beginning of all boundary layer measurements, the precision at which this could be accomplished was within approximately 0.005".

Table 3. Boundary Layer Thickness at Varying Configurations, x-locations, and Angle of Attack

Angle of Attack (degrees)	**Baseline**		**Thermocouple Wire at (2,3)**		**Thermocouple Wire at (2,3)**	
	x/c=0.12	**x/c=0.25**	**x/c=0.12**	**x/c=0.25**	**x/c=0.12**	**x/c=0.25**
14	1.51"	1.72"	3.09"	2.57"	2.25"	2.15"
16	1.98"	2.78"	3.41"	1.83"	2.78"	2.46"

Chapter 5

CONCLUSIONS AND RECOMMENDATIONS

Conclusions

A simple flow control technique was employed to evaluate the effects of cylinder in a crossflow on the laminar separation bubble over a generic airfoil. Flow over the model of known curvature airfoil was manipulated by two different size cylinders located upstream of the leading edge and the characteristics of the leading edge separation bubble and downstream separation were compared with that of an unmodified configuration. The flow Reynolds number (based on chord) was in the range of 27,000 to 45,000 over the model at angles of attack of 14, 16, and 18 degrees.

1. The length and height of the laminar separation bubble was found to be reduced with a small cylindrical wire placed at upstream locations defined by (2,3) and (2,5) at Reynolds number of 27,00. The same configuration showed a slight increase in bubble length at the higher Reynolds number (45,000).
2. However, these changes did not result in a substantial or distinguishable improvement in the downstream separation point. Since it was difficult to detect a small change in the separation point, this is considered a conservative statement. However, a change in the separation point would likely result in a substantial change/improvement in the aerodynamic performance of a MAV.
3. The laminar separation bubble was found to be eliminated very nearly or completely eliminated when a thermocouple wire was placed upstream of the leading edge at locations defined by (1,2), (2,3) and (2,4). Although the elimination of the bubble alone would result in only a minor decrease in drag and increase in lift, also there would be a possible improvement in the stability of the leading edge stall and possible reduction or elimination in the hysteresis associated with stall. However, like the results for the cylindrical wire configuration, it appeared that there was not a significant gain in the fluid energy

near the surface of the model to result in a readily detectable improvement in the downstream separation point.

Recommendations

A first recommendation to further the understanding of this research would be to perform a complete unsteady analysis of the flow control process. Specifically, one should study the phase of the vortex shedding from the separation bubble and time the boundary layer velocity measurements such that they were completed during the same phase each time – this would facilitate comparison between phase related flow events. Next, using a higher powered laser would literally illuminate more details in the flow. This could improve the precision at which measurements from images are made. To improve the images further, using a state-of-the-art camera with higher level ISO setting (larger than 320, preferably about 1200) would assist in capturing better details of the flow. A higher ISO level will also enable the use of an even higher shutter speed. This in turn would result in getting high speed details (high shutter speed pictures of the fluid over the entire model) and help better distinguish between laminar and turbulent characteristics.

Because there was success in removing the laminar separation bubble with the configurations studied in this experiment, it would be interesting to see the effects of using both these passive flow control techniques in addition to a proven active flow control method of injecting energy into the boundary layer. Noticeable changes in lift and drag could then result in the downstream shift of the separation point.
Finally it is recommended that quantitative measurements be made using non-intrusive PIV measurements.

List of References

List of References

1. Horton, H.P., “A Semi-Empirical Theory for the Growth and Bursting of Laminar Separation Bubbles”, *Ministry of Technology Aeronautical Research Council Current Papers*, 1969.

2. Tani, I., “Low Speed Flows Involving Bubble Separations”, *Progress in Aeronautical Science,* Vol. 5, 1964.

3. Abbott, I.H., and Doenhoff, A.E., *Theory of Wing Sections*, Dover Publications 1959.

4. Brendel, M. and Mueller, T.J., “Boundary Layer Measurements on an Airfoil and Low Reynolds Numbers”, AIAA Paper 87-9495, 1987.

5. Lissaman, P.B.S., “Low Reynolds Number Airfoils”, *Annual Review of Fluid Mechanics,* 1983.

6. Unknown, “Miniature Aerial Vehicles Research”, http://www.defense-update.com/features/du-2-04/mav-darpa.htm

7. White, F.M., *Viscous Fluid Flow,* 3rd Edition, McGraw Hill, 2006

8. McMasters, J. H., Nordvik, R. H., Henderson, M. L., Sandvig, J. H., “Two airfoil sections designed for low Reynolds numbers”, *Tech Soaring,* 6(4):2-24, 1981.

9. Mueller, T.J., and Delaurier, J.D., “Aerodynamics of Small Vehicles”, *Annual Review of Fluid Mechanics* 2003.

10. Talay, Theodore A., “Introduction to the Aerodynamics of Flight”, Langley Research Center, Scientific and Technical Information Office of National Aeronautics and Space Administration, Washington, D.C. 1975.

11. Marchman, J.F., “Aerodynamic Testing at Low Reynolds Numbers”, *Journal of Aircraft,* Vol. 24, No 2, February 1987.

12. Donavan, F.J., and Selig, M.S., “Low Reynolds Number Airfoil Design and Wind Tunnel Testing at Princeton University”, *Proceedings of the Conference of Low Reynolds Number Aerodynamics,* Notre Dame, 1989.

13. Adrian, R.J., “Laser Velocimetry”, *Fluid Mechanics Measurements,* 2nd Edition, Taylor and Francis, 1996.

14. Tennekes, H., and Lumley, J.L., *A First Course in Turbulence*, Massachusetts Institute of Technology 1972.

15. Jensen, K.D., "Flow Measurements", *Journal of The Brazilian Society of Mechanical Science and Engineering,* Vol. 26, No4, 2004.

16. Mueller, T.J., *Fixed and Flapping Wing Aerodynamics for Micro Air Vehicle Applications*, American Institute of Aeronautics and Astronautics, 2001.

17. Shyy, W., Lian, Y., Tang, J., Viieru, D., Liu, H., *Aerodynamics of Low Reynolds Number Flyers,* Cambridge Aerospace Series, Cambridge University Press, 2008.

18. Nowak, D.K., Solies, U.P., "Wind-Tunnel Tests of a High Lift Generation and Stall/Spin Recovery System", *Journal of Aircraft,* Vol. 37, No.3, May-June 2000.

19. Aftergood, S., "Unmanned Aerial Vehicles", http://www.fas.org/irp/program/collect/UAS.htm.

20. Schlichting, H., Gersten, K., Mayes, K., Oertel, H., *Boundary Layer Theory*, Edition 8, Springer 2000

21. Tani, I., "History of Boundary Layer Theory", *Annual Review of Fluid Mechanics*, Vol. 9, 1977.

22. Lin, J.C.M., and Pauley, L.L., "Low-Reynolds-Number Separation on an Airfoil", *AIAA Journal,* Vol. 34, No 8, August 1996.

23. Michalchuk, W.R., "An Investigation of Different Golf Ball Dimple Flow Fields", University of Tennesee Space Institute Master's Thesis, December 2006.

24. www.answers.com/topic/boundarylayer.

25. "Resolution of Hot-Wire Anemometry Measurements", TSI Incorporated 2007, www.tsi.com.

Appendices

Appendix A – Detailed Drawings

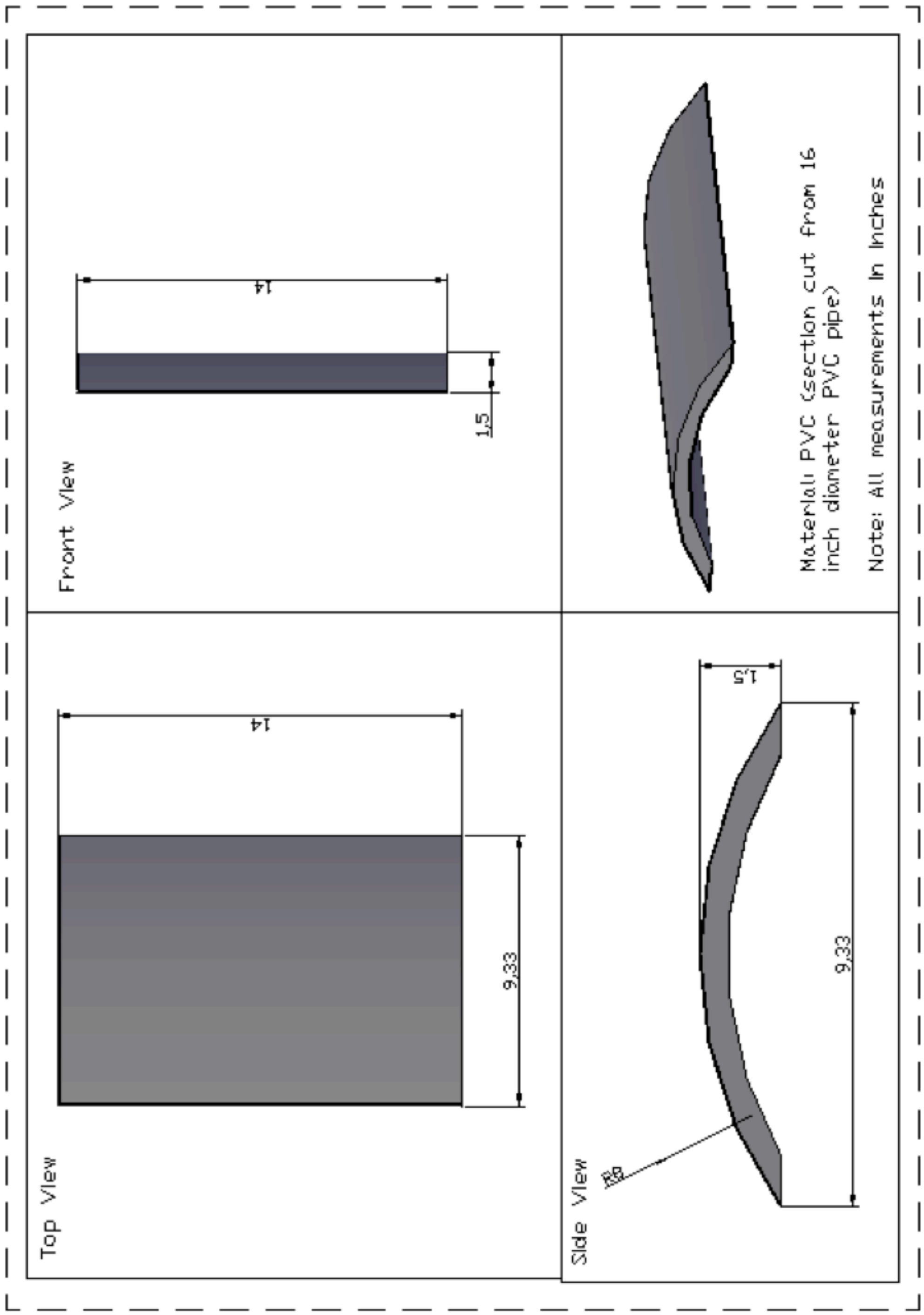

Figure 25. Detailed AutoCAD Drawings of Model

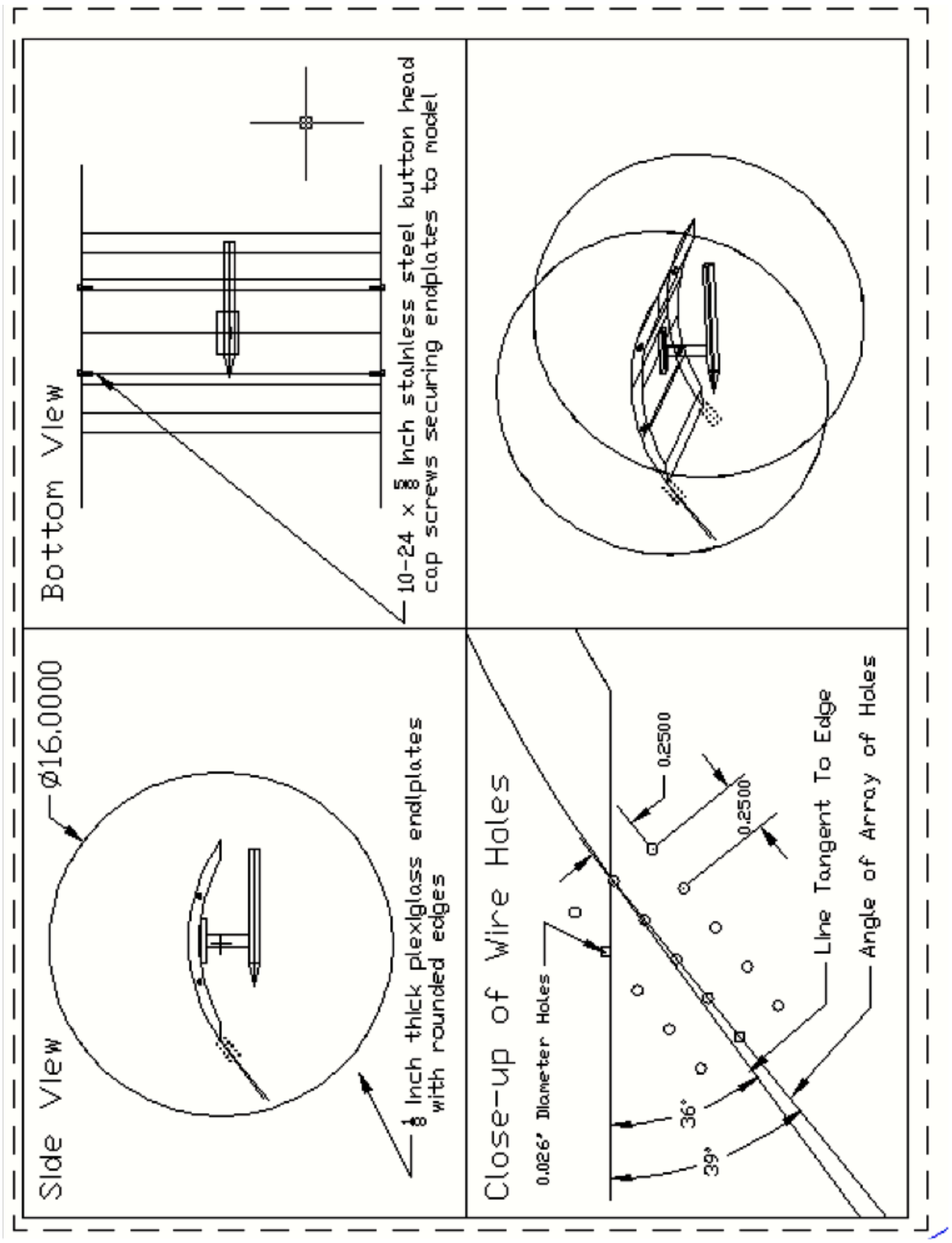

Figure 26. Detailed AutoCAD Drawings of Model, Endplates and Wire Holes

Appendix B – MATLAB Code

```
%Image Processing Scheme to View Details of the Leading Edge
Separation Bubble

%A batch of images are first read from the current directory
containing images with file names beginning with the characters
"B14"
files = dir('B14*.JPG');


%The "for" loop then crops each of the images, applies the
filter, segments the colours, shows the images for verification,
and then writes the new image data to a file name beginning with
"cropped\" followed by the original file name
for k = 1:numel(files)
    I = imread(files(k).name);
    CB=imcrop(I,[400 450 1830 825]);

    f=fspecial('motion');
    FB=imfilter(CB,f,'replicate');

    cform = makecform('srgb2lab');
    LB = applycform(FB,cform);

    ab = double(LB(:,:,2:3));
    nrows = size(ab,1);
    ncols = size(ab,2);
    ab = reshape(ab,nrows*ncols,2);
    nColors = 3;

    [IDX CC] = kmeans(ab,nColors,'distance', 'sqEuclidean');
    pixel_labels = reshape(IDX,nrows,ncols);

    segmented_images = cell(1,3);
    rgb_label = repmat(pixel_labels,[1 1 3]);

        for n = 1:nColors
            color = CB;
            color(rgb_label ~= n) = 0;
            segmented_images{n} = color;
        end


    SB=segmented_images{2};
    figure, imshow(SB)

    imwrite(SB, ['cropped\' files(k).name]);

end
```

```
%Image Processing Scheme to Determine Average Downstream
Separation Point

%A batch of images are first read from the current directory
containing
%images with file names beginning with the characters "G14"
files = dir('G14*.JPG');

%The "for" loop then crops each of the images, applies the
filters, shows the
%images for verification, and then writes the new image data to a
file name
%beginning with "cropped\" followed by the original file name
for k = 1:numel(files)
    I = imread(files(k).name);
    CG=imcrop(I,[90 659 1830 825]);

    f=fspecial('motion');
    FG=imfilter(CG,f,'replicate');

    f2=fspecial('average');
    SG=imfilter(FG,f2,'replicate');

    f3=fspecial('unsharp');
    SG=imfilter(SG,f3,'replicate');


    figure, imshow(SG)

    imwrite(SG, ['cropped\' files(k).name]);
end
```

Appendix C – Hot Film Sensor Calibration

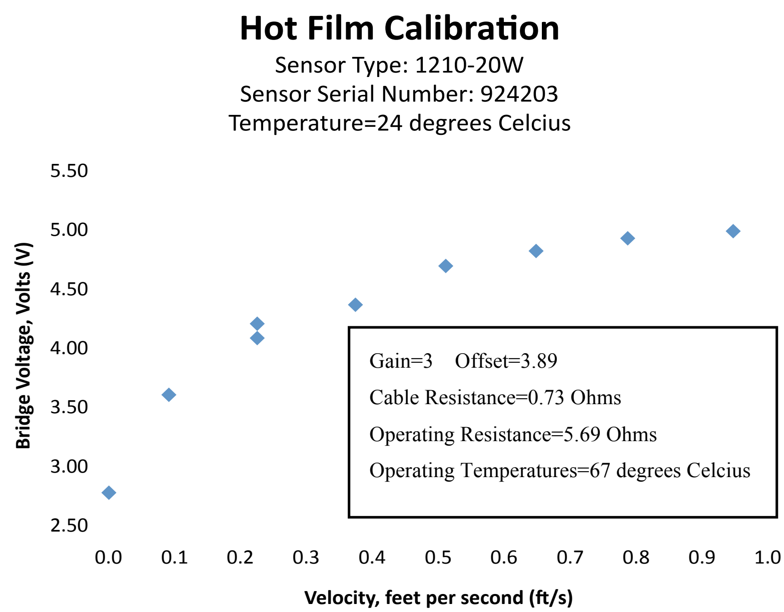

Figure 27. Hot Film Sensor Calibration at 24 degrees Celcius

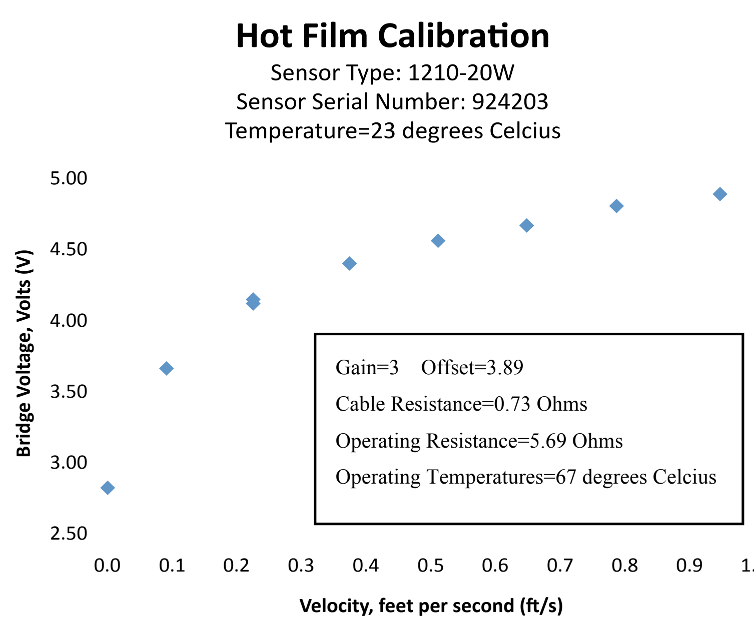

Figure 28. Hot Film Sensor Calibration at 23 degrees Celcius

Appendix D – Figures Referenced in Chapter 4

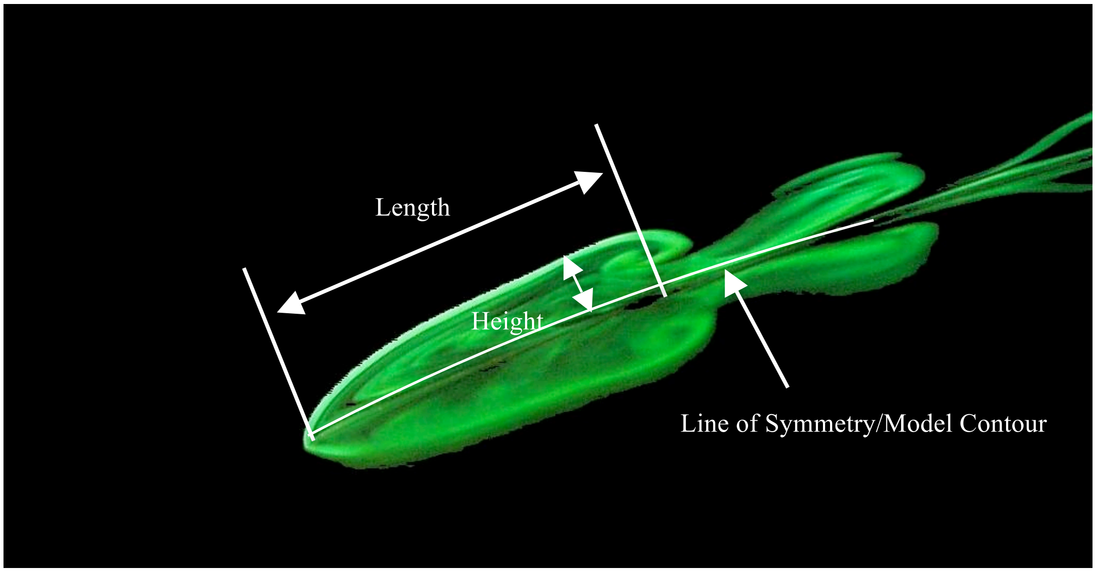

Figure 29. Measurement Details of the Laminar Separation Bubble

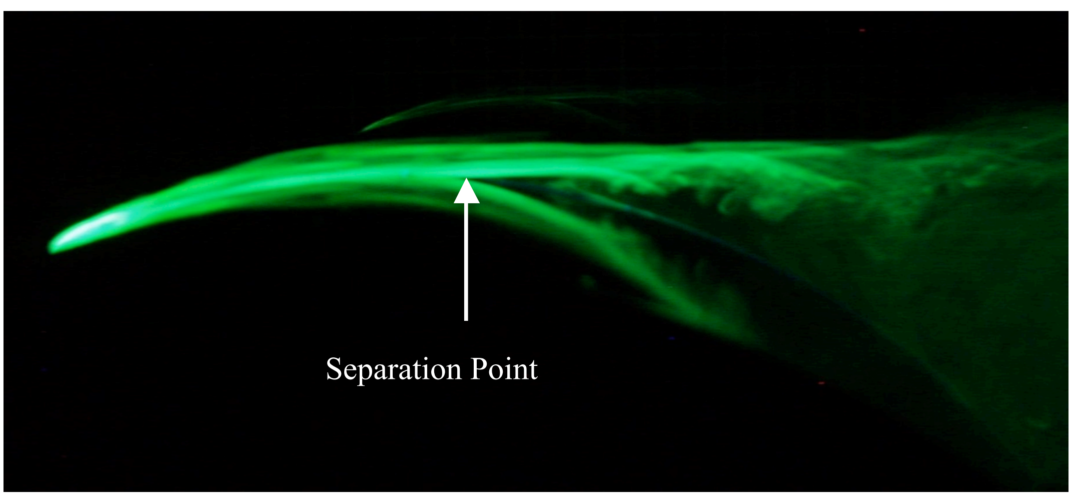

Figure 30. Measurement Details of the Downstream Separation Point

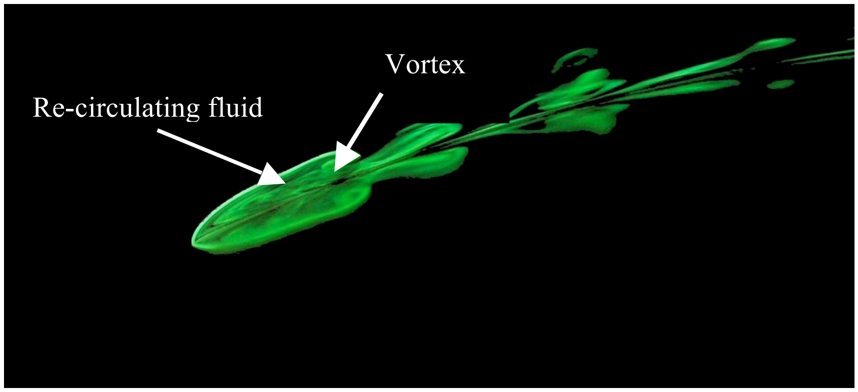

a. Length, x/c=0.023 ± 0.002; α=14 degrees

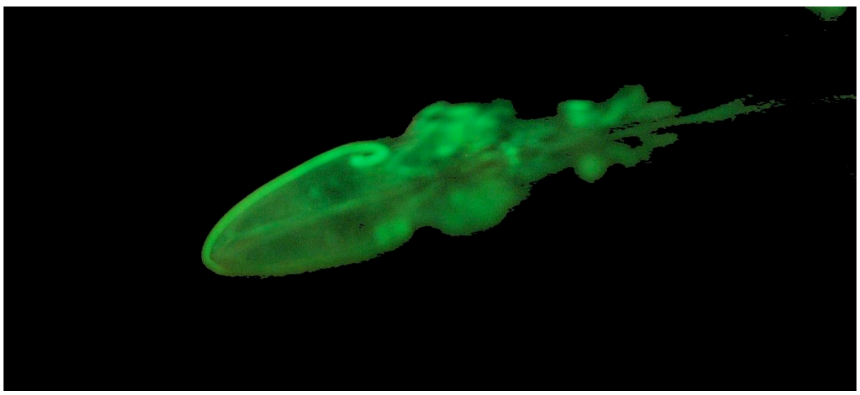

b. Length, x/c=0.030 ± 0.003; α=16 degrees

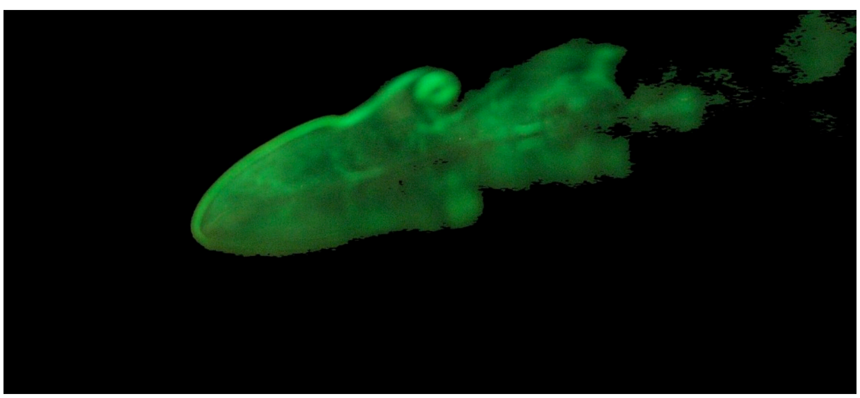

c. Length, x/c=0.028 ± 0.003; α=18 degrees

Figure 31. Comparison of the Laminar Separation Bubble at Three Angles of Attack at a Reynolds number of 27,000 (images are of the same scale)

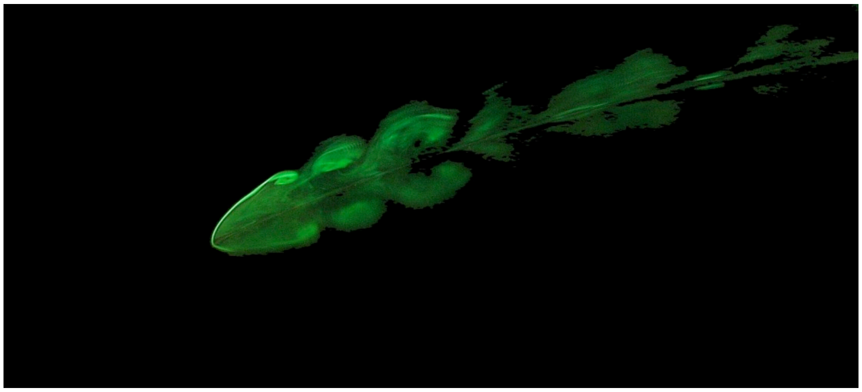

a. Length, x/c=0.016 ±0.002; α=14 degrees

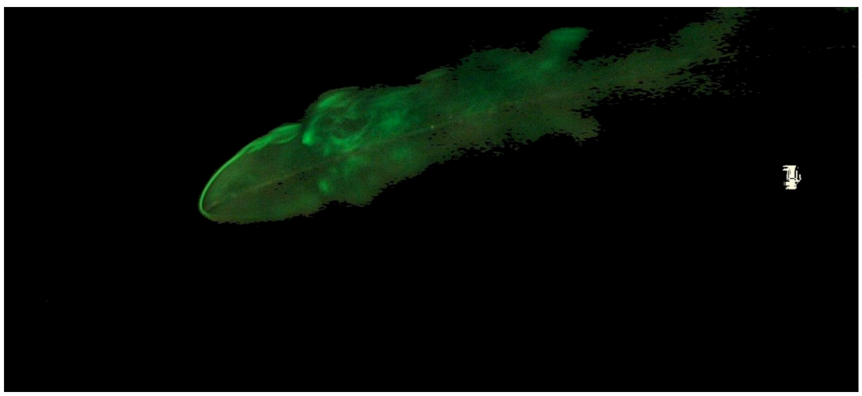

b. Length, x/c=0.016 ±0.003; α=16 degrees

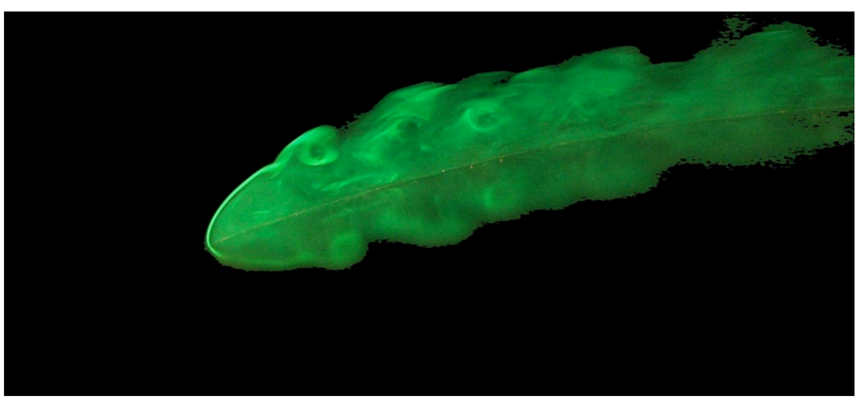

c. Length, x/c=0.018 ±0.004; α=18 degrees

Figure 32. Comparison of the Laminar Separation Bubble at Three Angles of Attack at a Reynolds number of 45,000 (images are of the same scale)

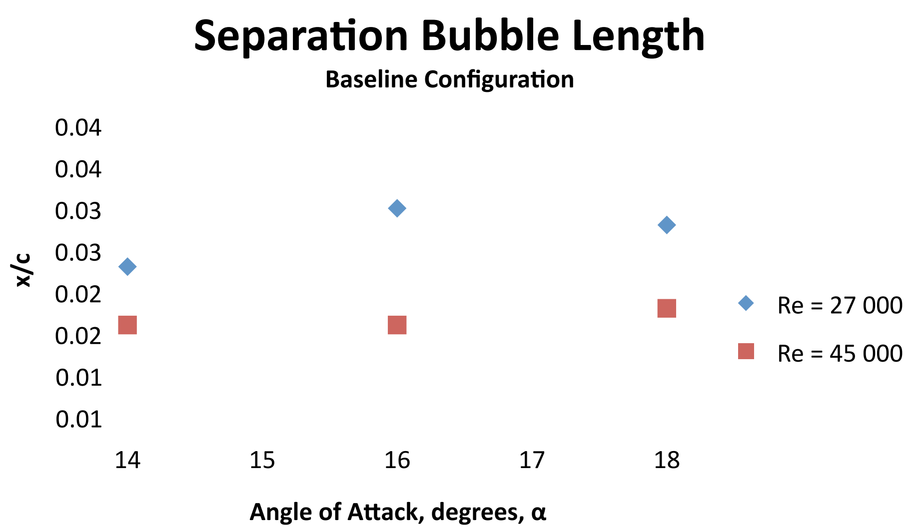

Figure 33. Comparison Of The Laminar Separation Bubble Length With Varying Reynolds Number And Angle Of Attack

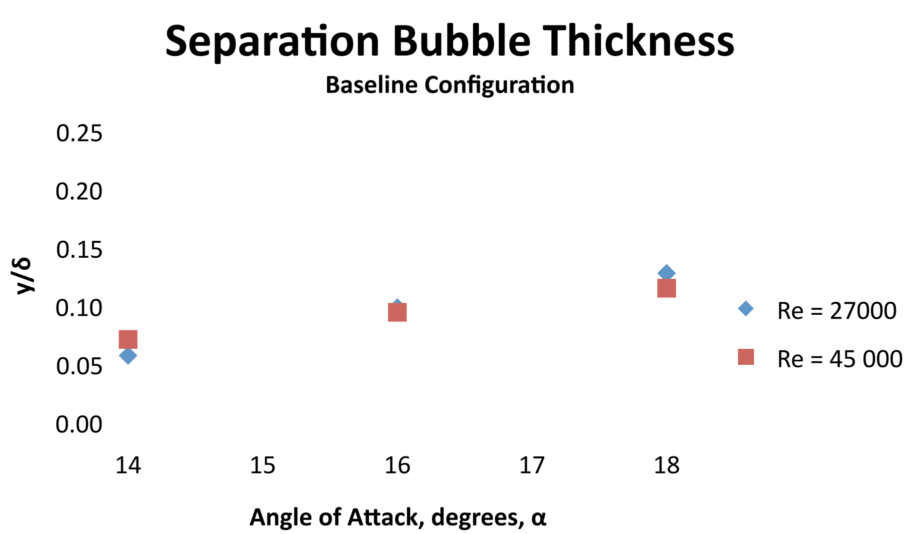

Figure 34. Comparison Of The Laminar Separation Bubble Thickness With Varying Reynolds Number And Angle Of Attack

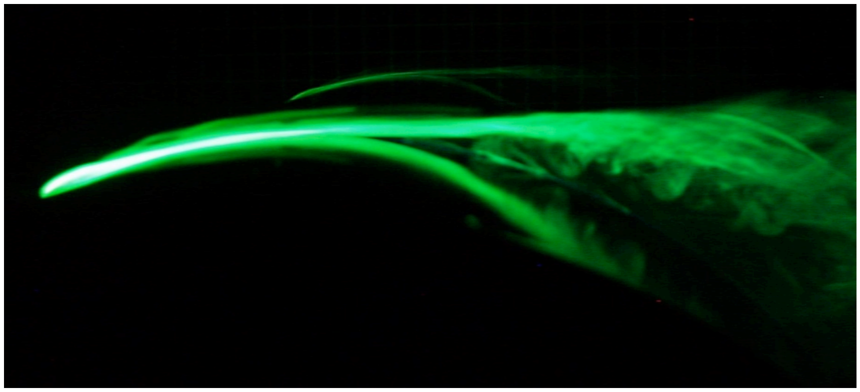

a. Separation Point, x/c=0.37 ±0.01; α=14 degrees

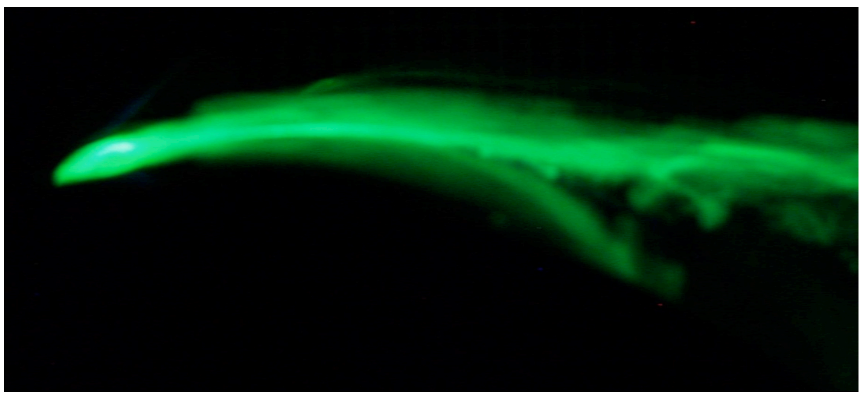

b. Separation Point, x/c=0.50 ± 0.03; α=16 degrees

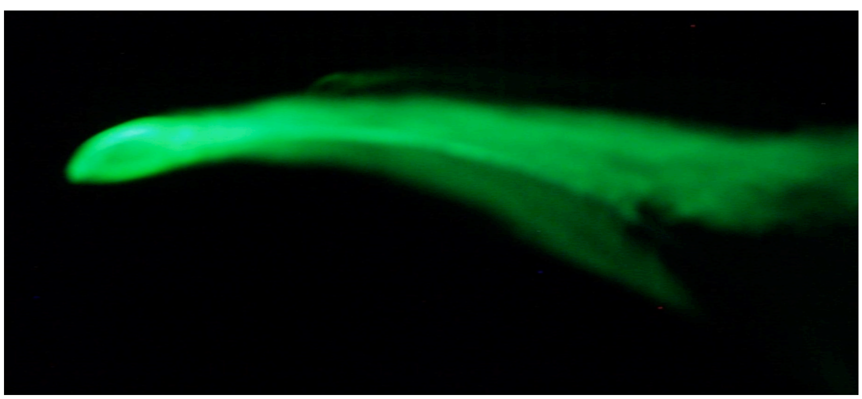

c. Separation Point, x/c=0.60 ± 0.12; α=18 degrees

Figure 35. Comparison Of The Downstream Separation Point At Three Angles Of Attack At A Reynolds Number Of 27,000 (images are of the same scale)

a. Separation Point, x/c=0.67 ± 0.03; α=14 degrees

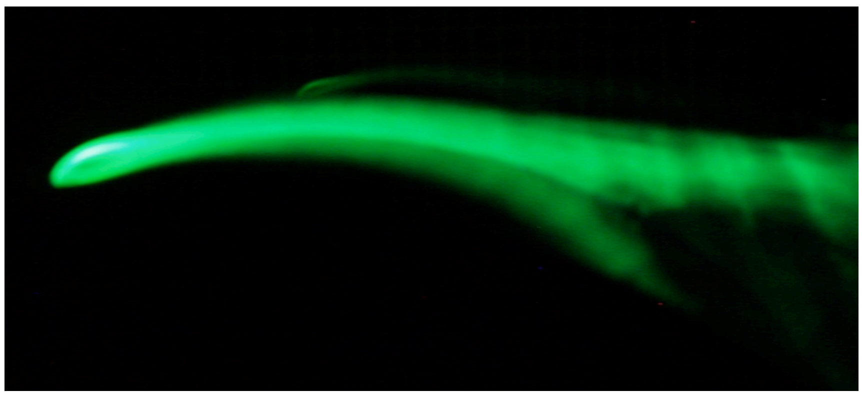

b. Separation Point, x/c=0.65 ± 0.03; α=16 degrees

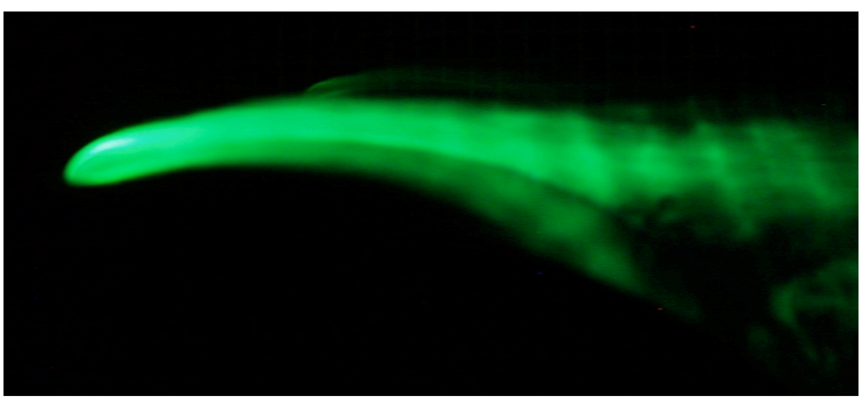

c. Separation Point, x/c=0.69 ± 0.04; α=18 degrees

Figure 36. Comparison Of The Downstream Separation Point At Three Angles Of Attack At A Reynolds Number Of 45,000 (images are of the same scale)

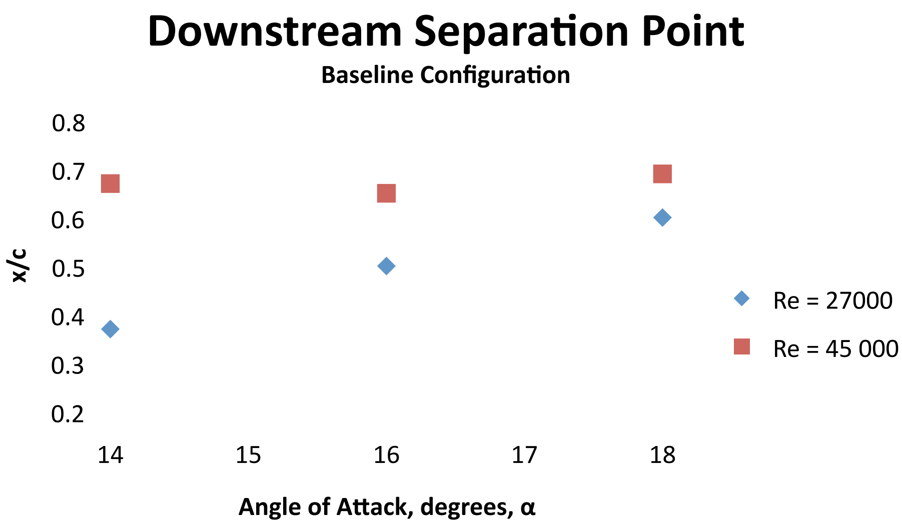

Figure 37. Comparison Of The Downstream Separation Point With Varying Reynolds Number And Angle Of Attack in The Baseline Configuration

a. Baseline configuration, length x/c=0.023 ± 0.002

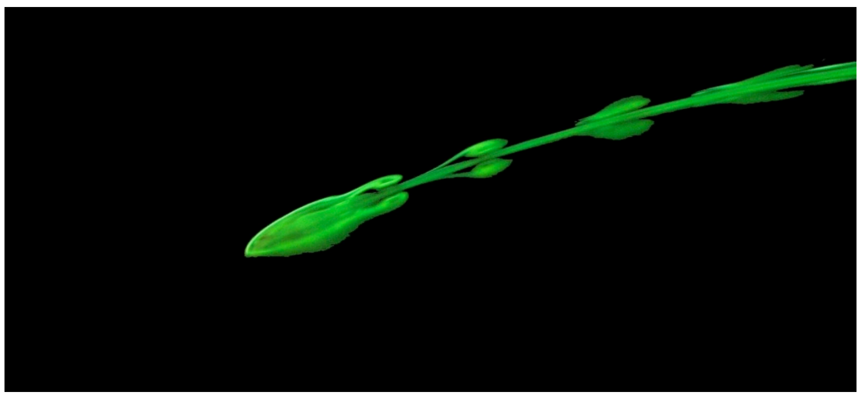

b. Cylindrical Wire located at (2,3), length x/c=0.016 ±0.002

c. Cylindrical Wire located at (2,5), length x/c=0.021 ±0.003

Figure 38. Comparison Of The Laminar Separation Bubbles With Cylindrical Wires Placed At Varying Upstream Locations At An Angle Of Attack Of 14 Degrees And A Reynolds Number Of 27,000 (images are of the same scale)

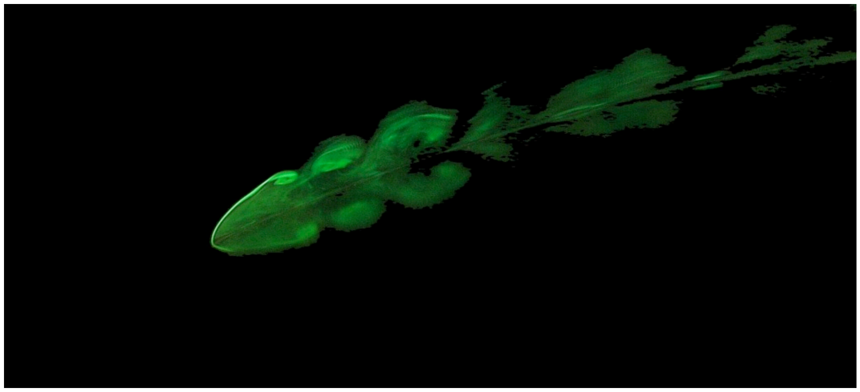

a. Baseline configuration, length x/c=0.016 ± 0.002

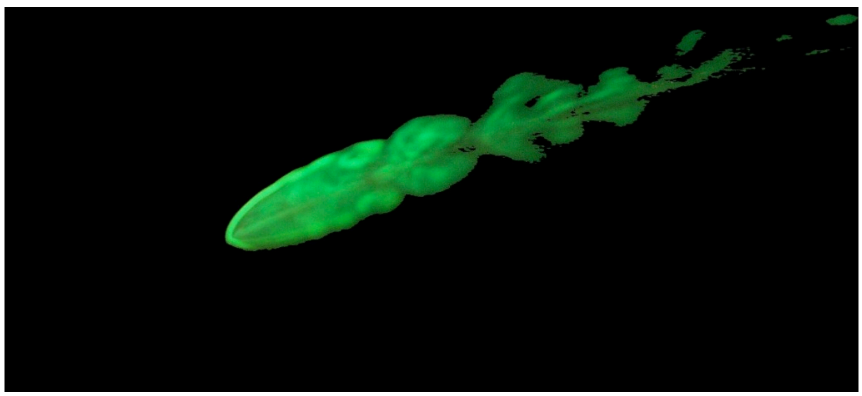

b. Cylindrical Wire at (2,3), length x/c=0.021 ± 0.003

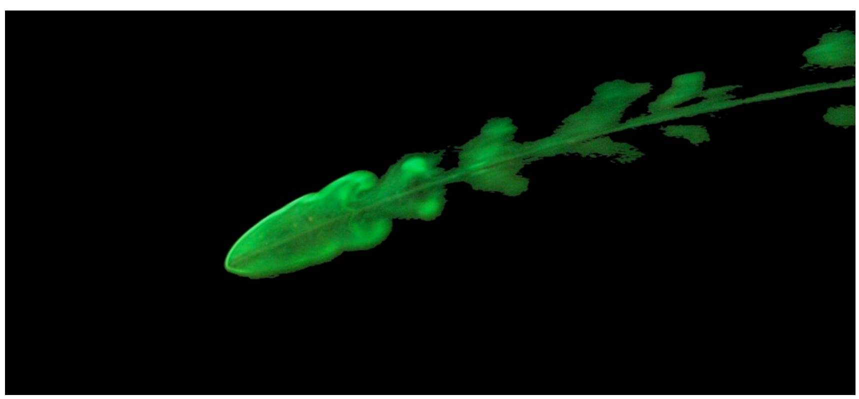

c. Cylindrical Wire at (2,5), length x/c=0.022 ±0.003

Figure 39. Comparison Of The Laminar Separation Bubbles With Cylindrical Wires Placed At Varying Upstream Locations At An Angle Of Attack Of 14 Degrees And A Reynolds Number Of 45,000 (images are at the same scale)

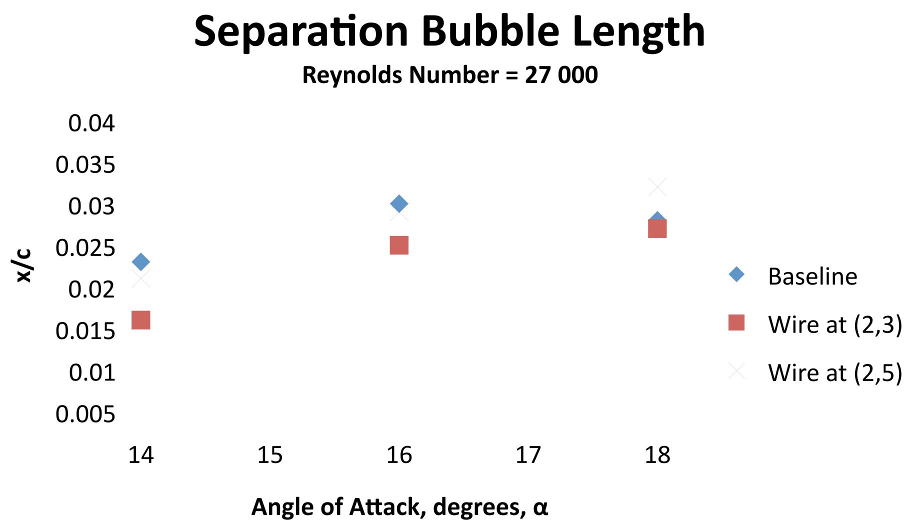

Figure 40. Comparison Of The Separation Bubble Length With A Cylindrical Wire Placed At Varying Locations Upstream Of The Leading Edge At A Reynolds Number Of 27,000

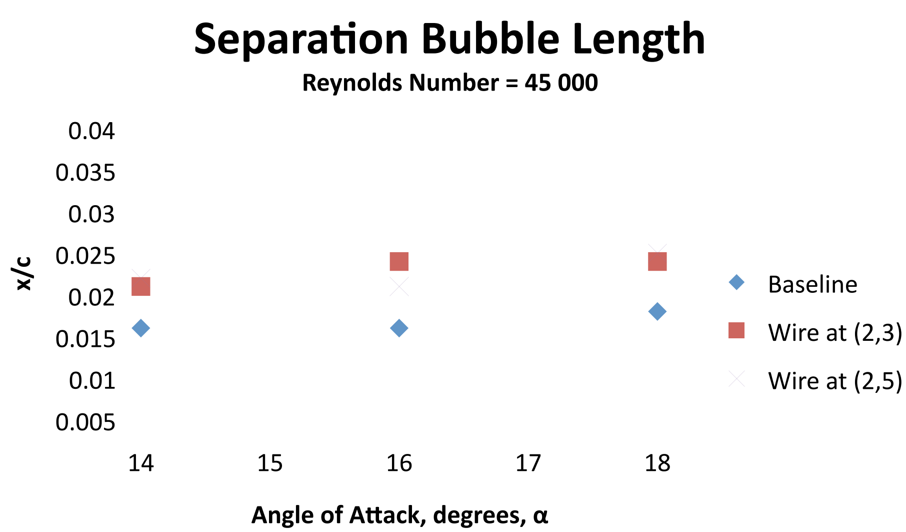

Figure 41. Comparison Of The Separation Bubble Length With A Cylindrical Wire Placed At Varying Locations Upstream Of The Leading Edge At A Reynolds Number Of 45,000

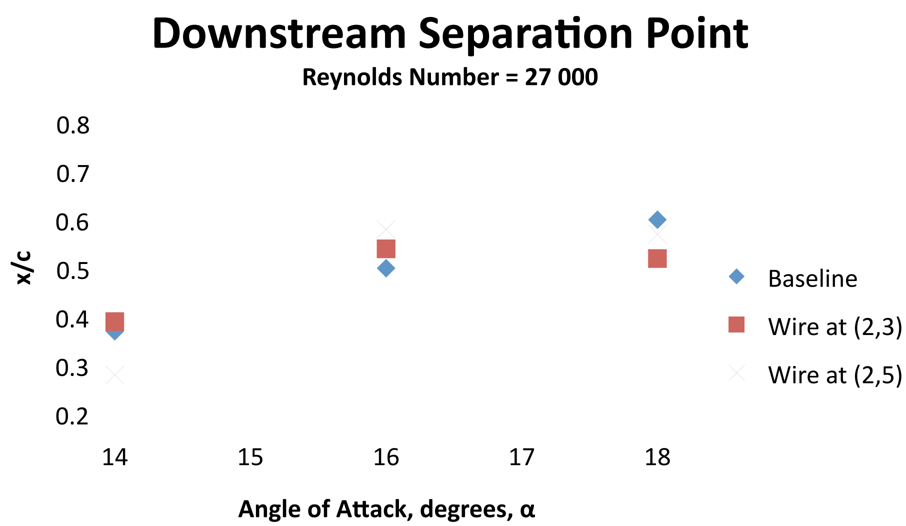

Figure 42. Comparison Of The Downstream Separation Point With A Cylindrical Wire Placed At Varying Locations Upstream Of The Leading Edge At A Reynolds Number Of 27,000

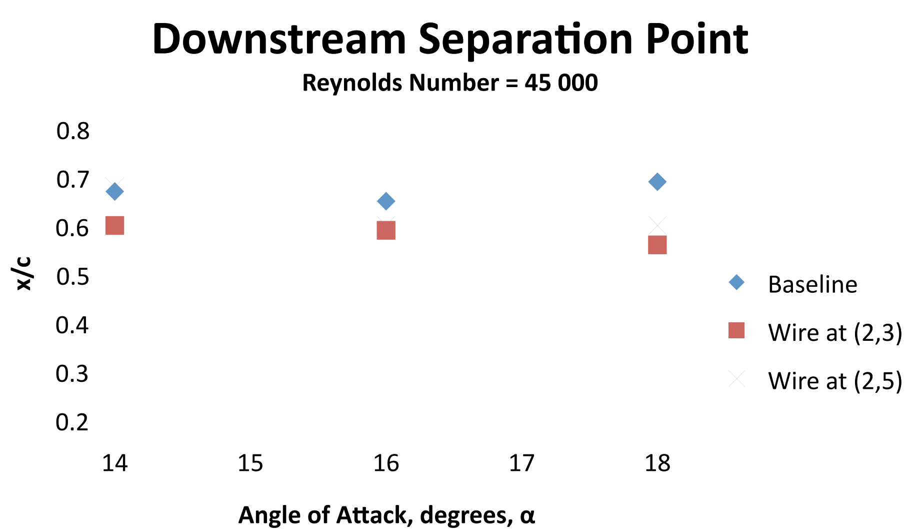

Figure 43. Comparison Of The Downstream Separation Point With A Cylindrical Wire Placed At Varying Locations Upstream Of The Leading Edge At A Reynolds Number Of 27,000

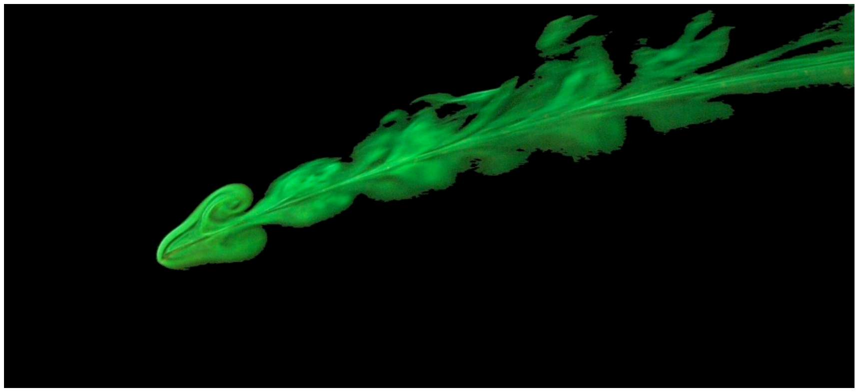

a. Thermocouple Wire at (1,2)

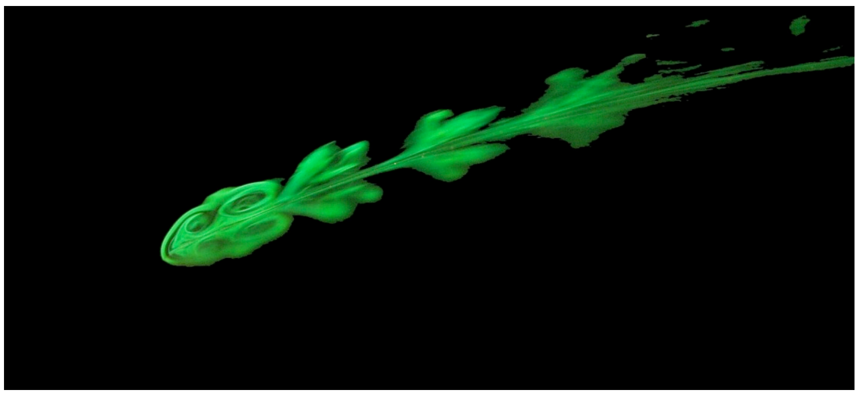

b. Thermocouple Wire at (2,3)

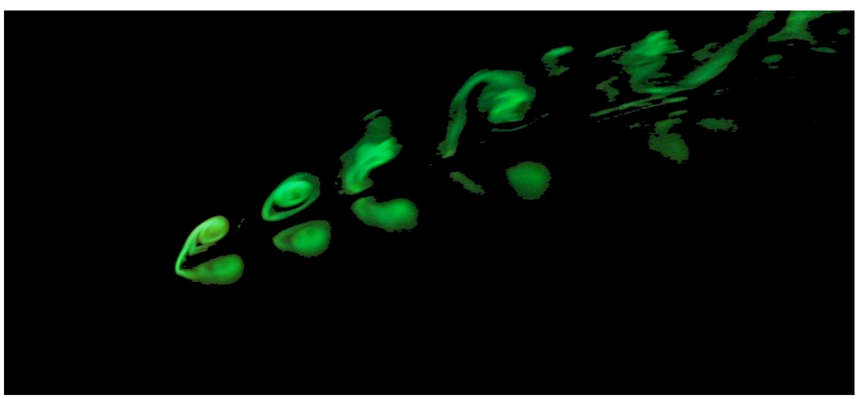

c. Thermocouple Wire at (2,4)

Figure 44. Comparison Of Leading Edge Flow With Thermocouple Wire Placed Upstream, At An Angle Of Attack Of 14 Degrees, And Reynolds Number Of 27,000

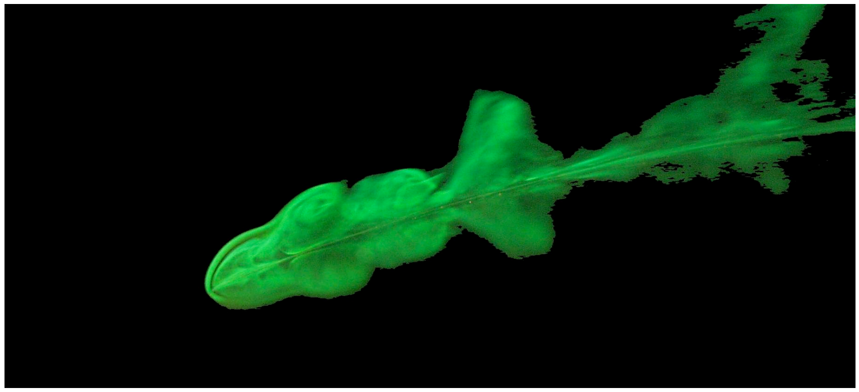

a. Thermocouple Wire at (1,2)

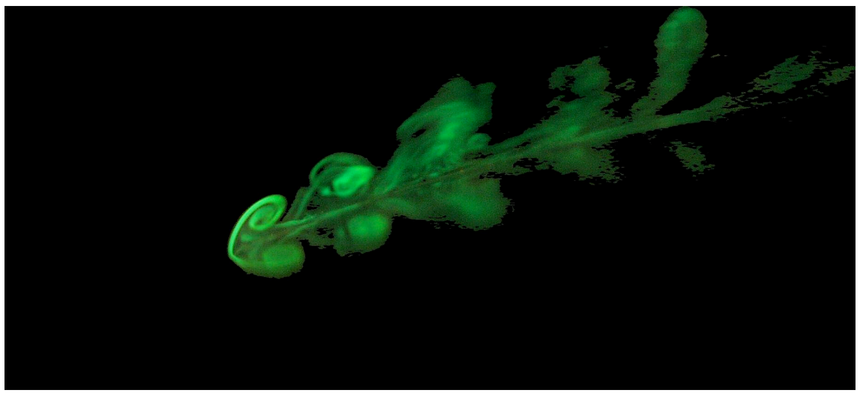

b. Thermocouple Wire at (2,3)

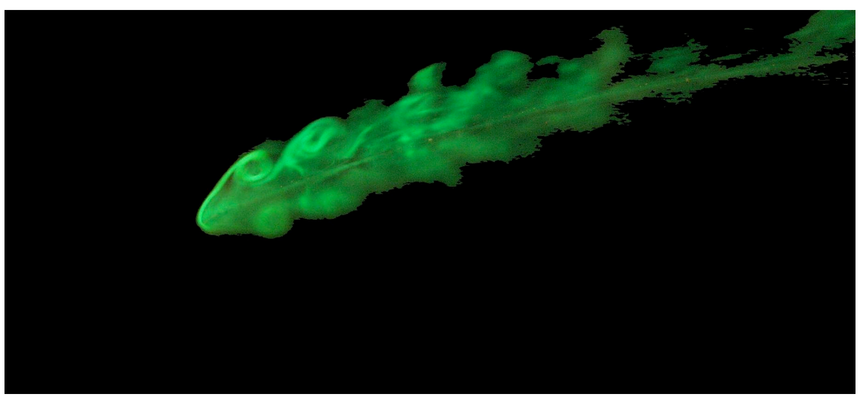

c. Thermocouple Wire at (2,4)

Figure 45. Comparison Of Leading Edge Flow With Thermocouple Wire Placed Upstream, At An Angle Of Attack Of 16 Degrees, And Reynolds Number Of 27,000

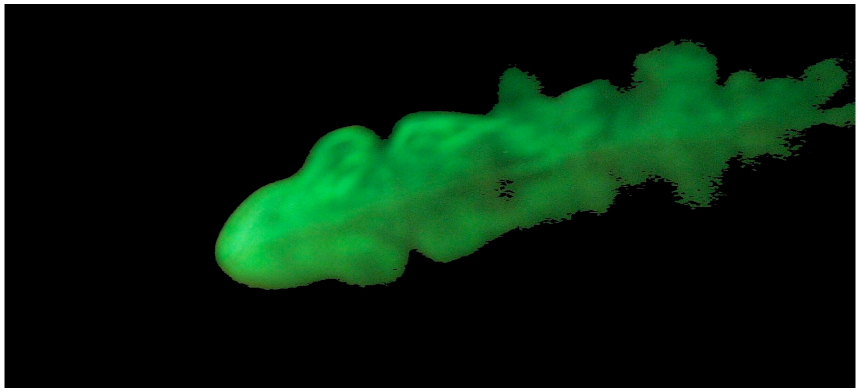

a. Thermocouple Wire at (1,2)

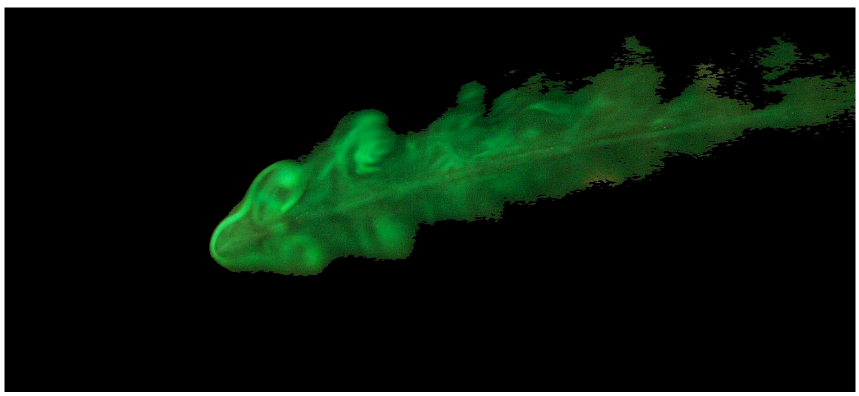

b. Thermocouple Wire at (2,3)

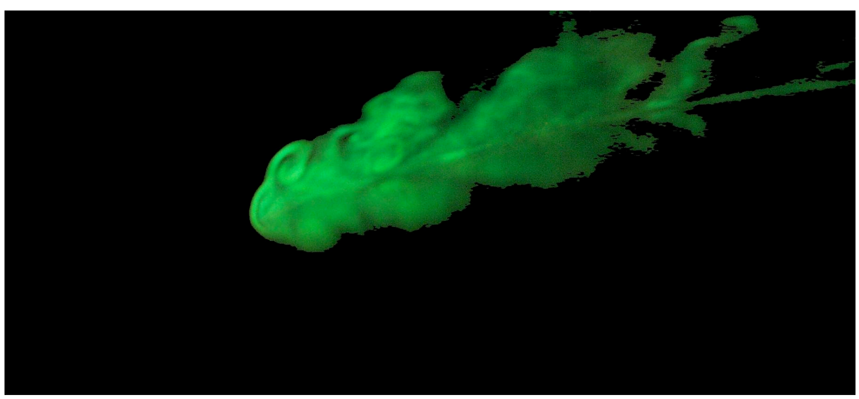

c. Thermocouple Wire at (2,4)

Figure 46. Comparison Of Leading Edge Flow With Thermocouple Wire Placed Upstream, At An Angle Of Attack Of 18 Degrees, And Reynolds Number Of 27,000

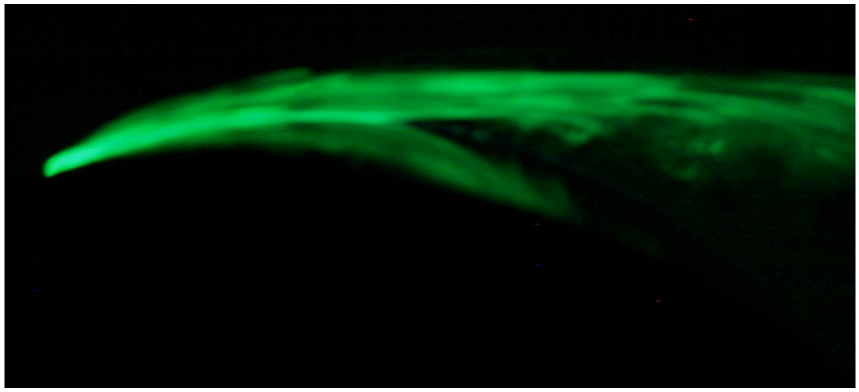

a. Thermocouple Wire at (1,2), Separation Point at x/c=0.42 ± 0.02

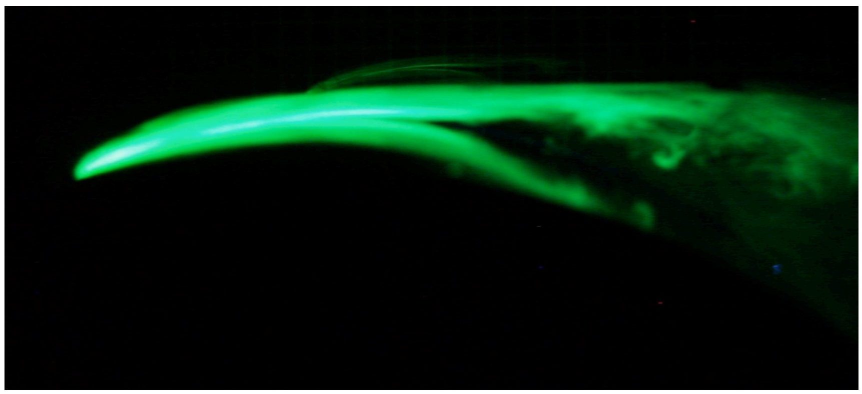

b. Thermocouple Wire at (2,3), Separation Point at x/c=0.39 ± 0.03

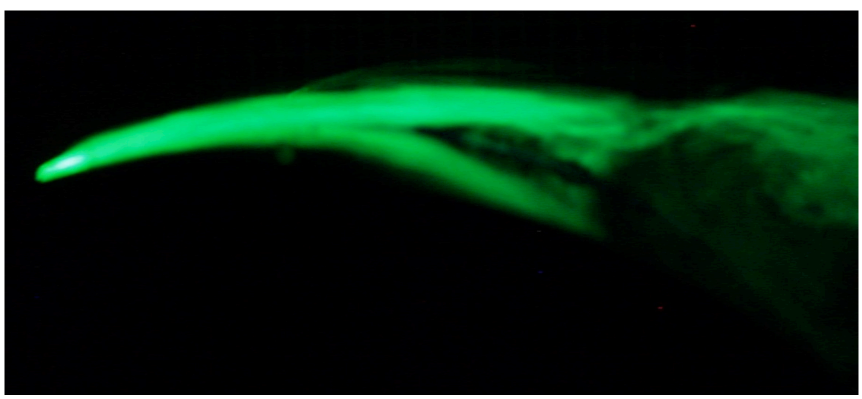

c. Thermocouple Wire at (2,4), Separation Point at x/c=0.43 ± 0.01

Figure 47. Comparison Of Downstream Separation With Thermocouple Wire Upstream, At An Angle Of Attack Of 14 Degrees And Reynolds Number Of 27,000

a. Thermocouple Wire at (1,2), Separation Point at x/c=0.55 ± 0.03

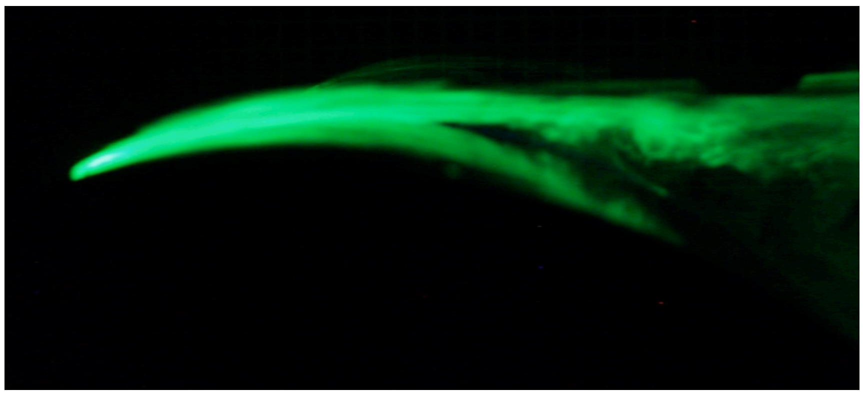

b. Thermocouple Wire at (2,3), Separation Point at x/c=0.42 ± 0.01

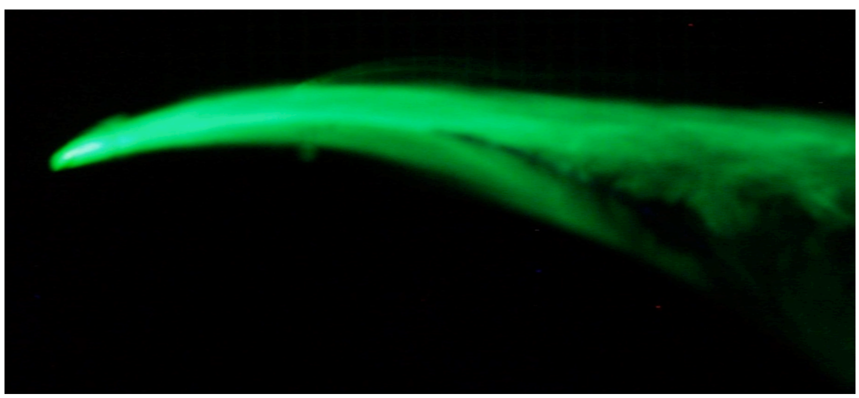

c. Thermocouple Wire at (2,4), Separation Point at x/c=0.56 ± 0.07

Figure 48. Comparison Of Downstream Separation With Thermocouple Wire Upstream, At An Angle Of Attack Of 16 Degrees And Reynolds Number Of 27,000

a. Thermocouple Wire at (1,2), Separation Point at x/c=0.54 ± 0.02

b. Thermocouple Wire at (2,3), Separation Point at x/c=0.52 ± 0.08

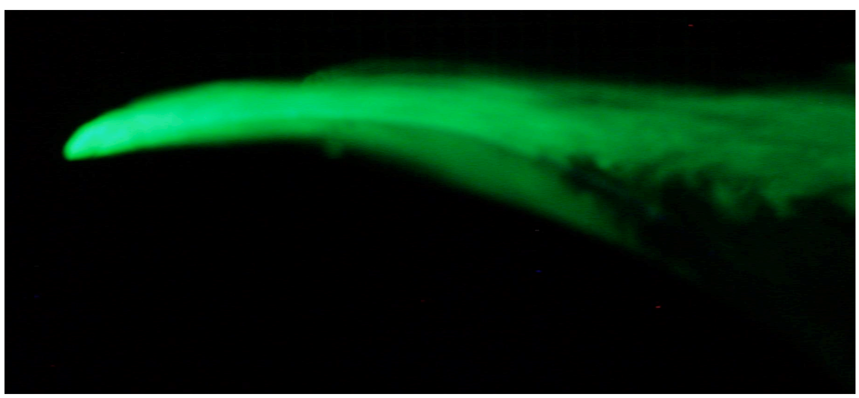

c. Thermocouple Wire at (2,4), Separation Point at x/c=0.61 ± 0.08

Figure 49. Comparison Of Downstream Separation With Thermocouple Wire Upstream, At An Angle Of Attack Of 18 Degrees And Reynolds Number Of 27,000

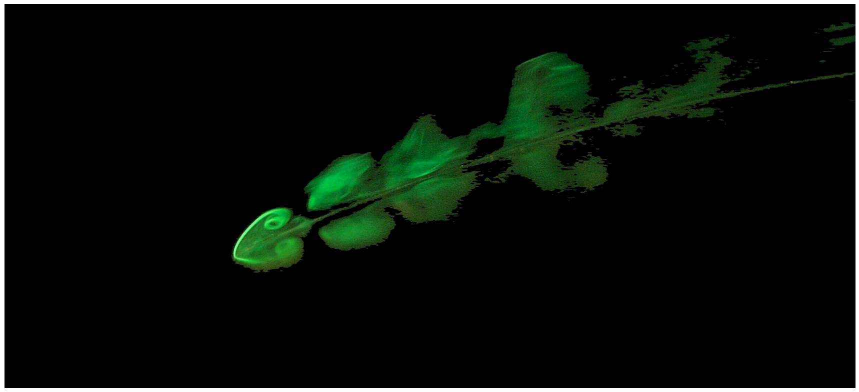

a. Thermocouple Wire at (1,2)

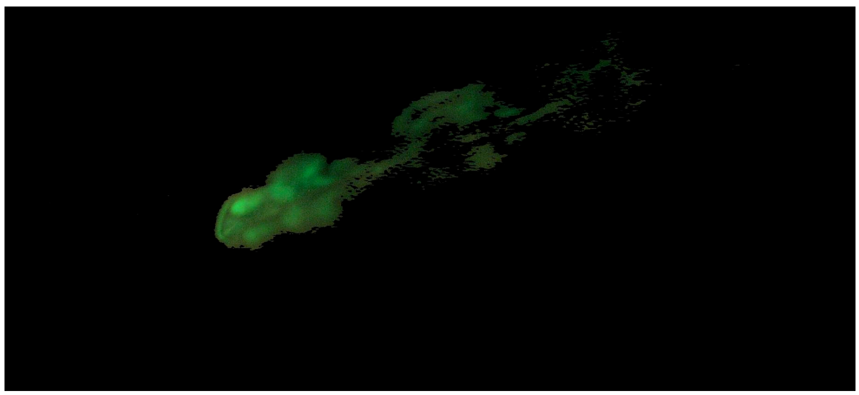

b. Thermocouple Wire at (2,3)

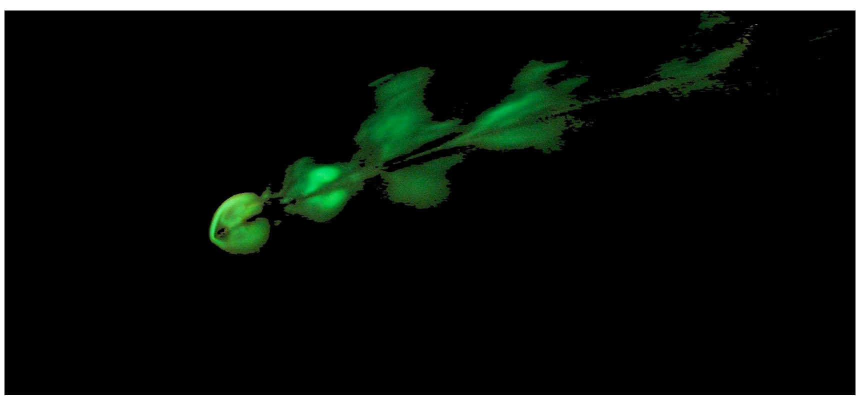

c. Thermocouple Wire at (2,4)

Figure 50. Comparison Of Leading Edge Flow With Thermocouple Wire Placed Upstream, At An Angle Of Attack Of 14 Degrees, And Reynolds Number Of 45,000

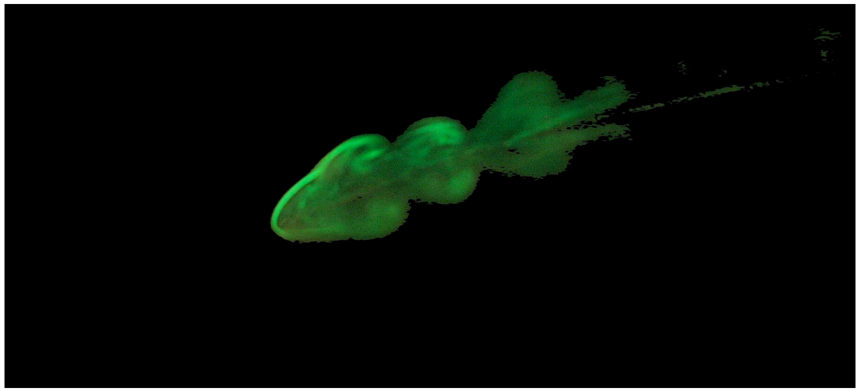

a. Thermocouple Wire at (1,2)

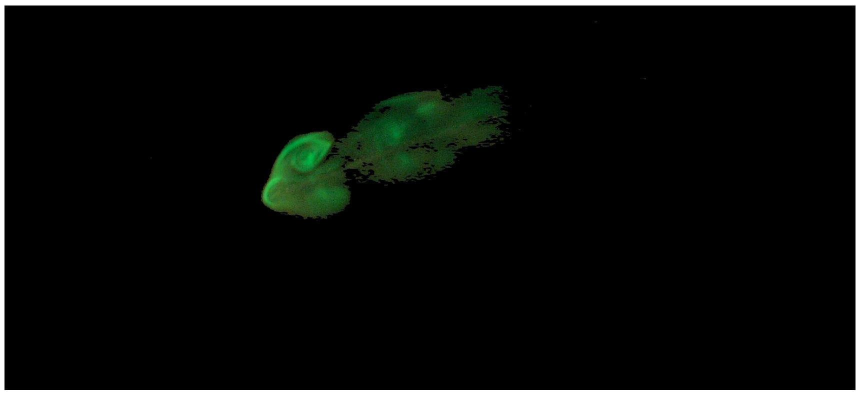

b. Thermocouple Wire at (2,3)

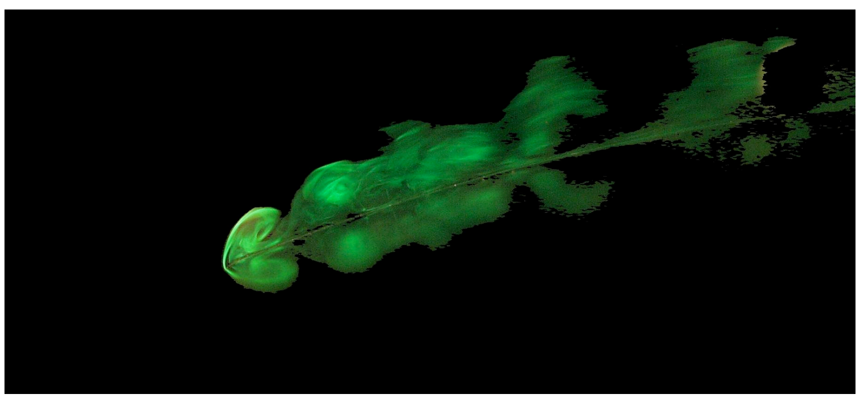

c. Thermocouple Wire at (2,4)

Figure 51. Comparison Of Leading Edge Flow With Thermocouple Wire Placed Upstream, At An Angle Of Attack Of 16 Degrees, And Reynolds Number Of 45,000

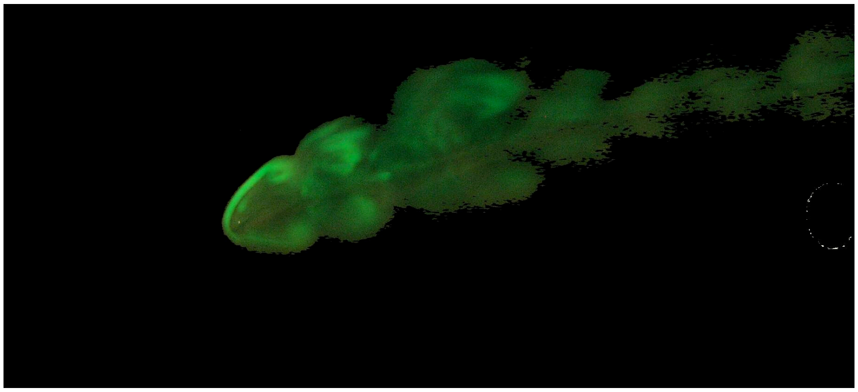

a. Thermocouple Wire at (1,2)

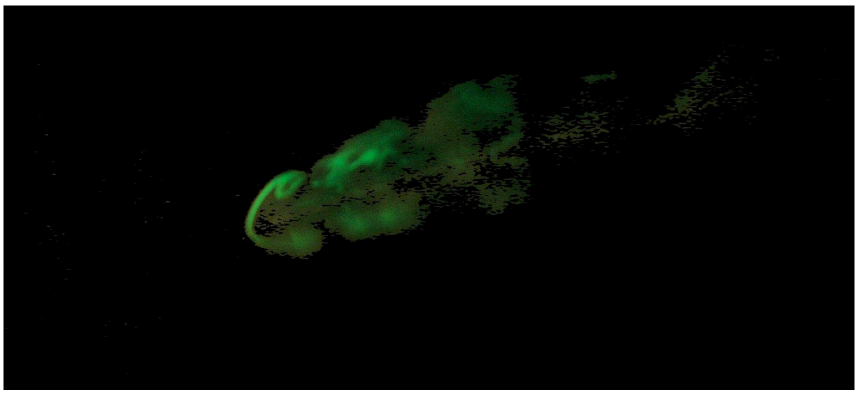

b. Thermocouple Wire at (2,3)

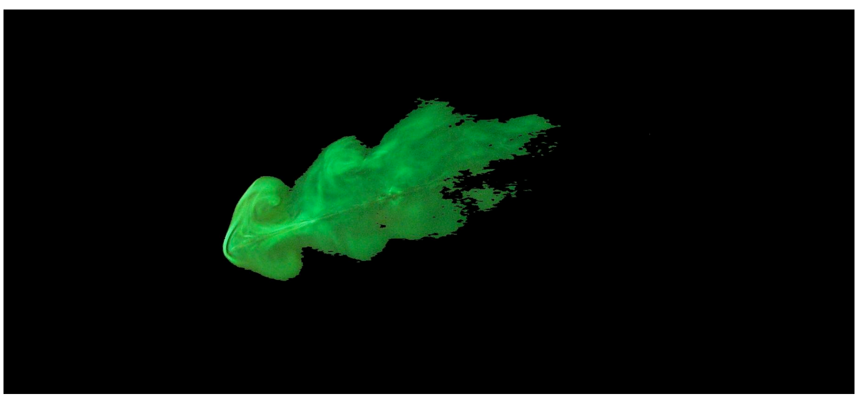

c. Thermocouple Wire at (2,4)

Figure 52. Comparison Of Leading Edge Flow With Thermocouple Wire Placed Upstream, At An Angle Of Attack Of 18 Degrees, And Reynolds Number Of 45,000

a. Thermocouple Wire at (1,2), Separation Point at x/c=0.64 ± 0.06

b. Thermocouple Wire at (2,3), Separation Point at x/c=0.71 ± 0.05

c. Thermocouple Wire at (2,4), Separation Point at x/c=0.65 ± 0.08

Figure 53. Comparison Of Downstream Separation With Thermocouple Wire Upstream, At An Angle Of Attack Of 14 Degrees And Reynolds Number Of 45,000

a. Thermocouple Wire at (1,2), Separation Point at x/c=0.62 ± 0.08

b. Thermocouple Wire at (2,3), Separation Point at x/c=0.69 ± 0.05

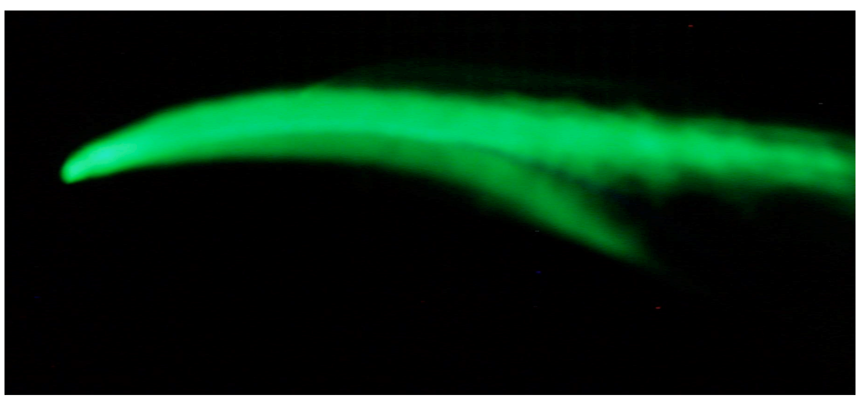

c. Thermocouple Wire at (2,4), Separation Point at x/c=0.60 ± 0.05

Figure 54. Comparison Of Downstream Separation With Thermocouple Wire Upstream, At An Angle Of Attack Of 16 Degrees And Reynolds Number Of 45,000

a. Thermocouple Wire at (1,2), Separation Point at x/c=0.60 ± 0.04

b. Thermocouple Wire at (2,3), Separation Point at x/c=0.59 ± 0.03

c. Thermocouple Wire at (2,4), Separation Point at x/c=0.54 ± 0.02

Figure 55. Comparison Of Downstream Separation With Thermocouple Wire Upstream, At An Angle Of Attack Of 18 Degrees And Reynolds Number Of 45,000

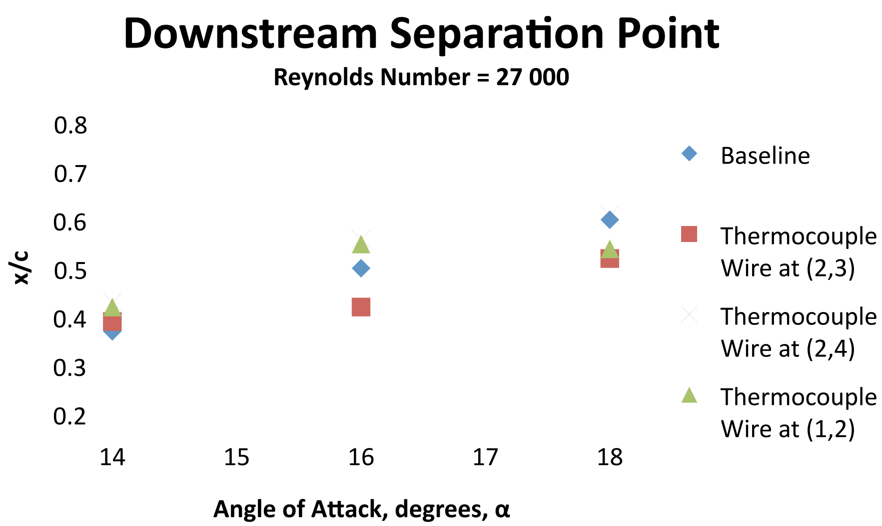

Figure 56. Comparison Of The Downstream Separation Point With A Thermocouple Wire Placed At Varying Locations Upstream Of The Leading Edge At A Reynolds Number Of 27,000

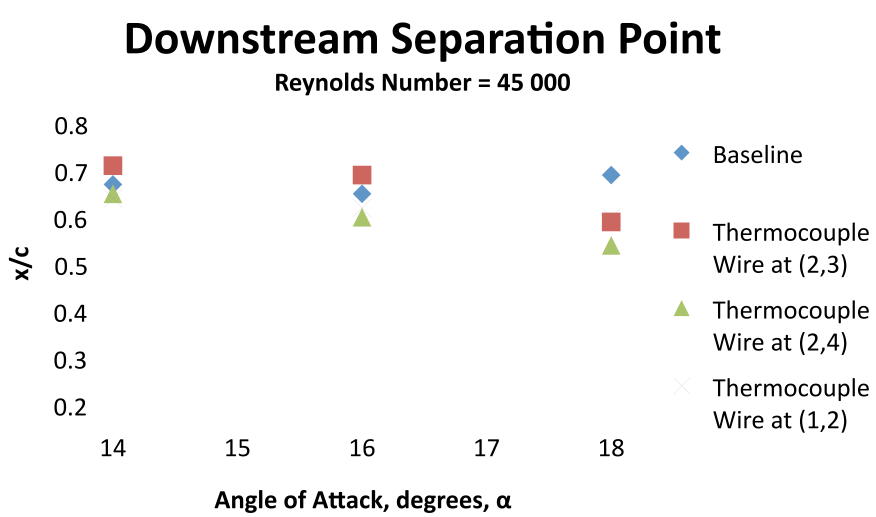

Figure 57. Comparison Of The Downstream Separation Point With A Thermocouple Wire Placed At Varying Locations Upstream Of The Leading Edge At A Reynolds Number Of 45,000

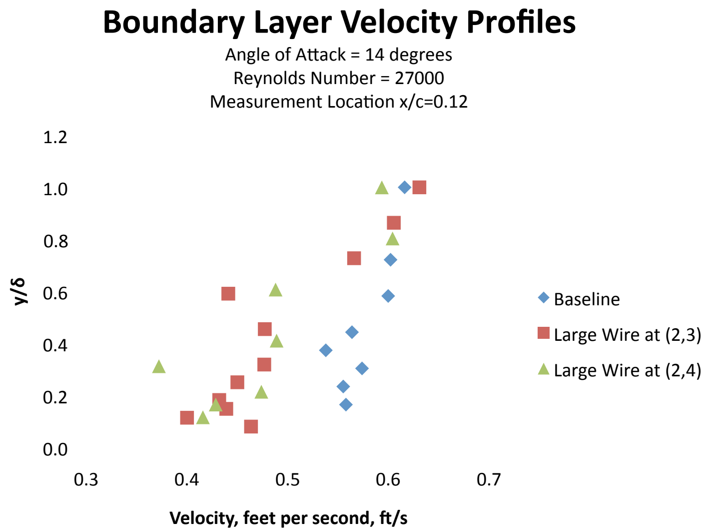

Figure 58. Boundary Layer Velocity Profiles at Reynolds number 27,000, Angle of Attack 14 Degrees and x/c=0.12

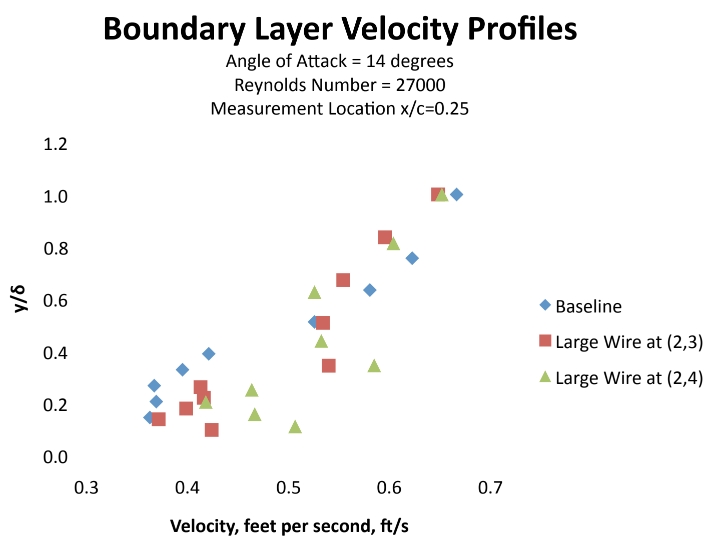

Figure 59. Boundary Layer Velocity Profiles at Reynolds number 27,000, Angle of Attack 14 Degrees and x/c=0.25

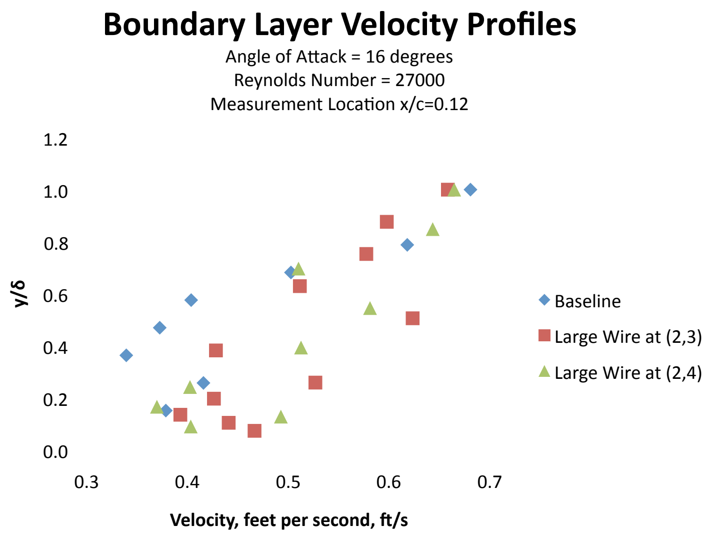

Figure 60. Boundary Layer Velocity Profiles at Reynolds number 27,000, Angle of Attack 16 Degrees and x/c=0.12

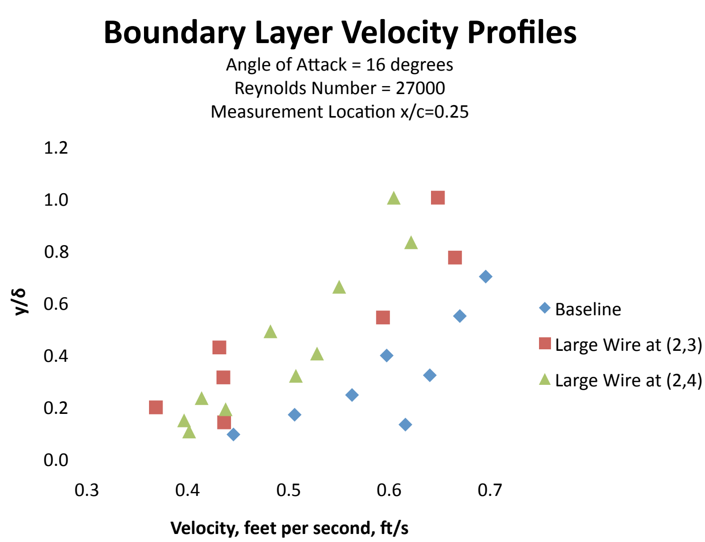

Figure 61. Boundary Layer Velocity Profiles at Reynolds number 27,000, Angle of Attack 16 Degrees and x/c=0.25

Vita

Karla Marie Swift was born in Stephenville, Newfoundland and Labrador, Canada on October 8, 1979. She was raised in Kippens, Newfoundland and graduated from St. Stephen's High School in 1997. From there she enrolled in the Canadian Forces in the Aerospace Engineering Officer (AERE) occupation, completed Basic Training in St Jean, Quebec and began studies at the Royal Military College of Canada in Kingston, Ontario. She graduated with a Bachelor of Science Degree in Mechanical Engineering in May 2001 and was subsequently promoted to Second Lieutenant. Upon completion of the AERE Officer Basic Course in May 2002, she was promoted to Lieutenant and posted to 14 Air Maintenance Squadron in Greenwood, Nova Scotia where she held the positions of Line Servicing Officer, Engineering Support Officer, and, after being promoted to Captain in 2004, the Deputy Aircraft Maintenance Support Officer. In 2005, she was posted to the Canadian Forces School of Aerospace Technology and Engineering where she served as an instructor on the AERE Basic Course and as coordinator of the AERE Practical Phase Training Program. She began studies at the University of Tennessee Space Institute in August 2007 completing all requirements for the degree of Master of Science in Aerospace Engineering. After completion of her studies she will be posted to the Aerospace Engineering Test Establishment in Cold Lake, Alberta.

In her spare time, Karla enjoys swimming, playing soccer and hiking with her husband and dogs. She is married to Corporal David Swift of Orangeville, Ontario, Canada.